

Non-linear fitting with joint spatial regularization in Arterial Spin Labeling

Oliver Maier^a, Stefan M Spann^a, Daniela Pinter^b, Thomas Gattringer^{b,c}, Nicole Hinteregger^c, Gerhard G. Thallinger^{d,e}, Christian Enzinger^{b,c}, Josef Pfeuffer^f, Kristian Bredies^{g,e}, Rudolf Stollberger^{a,e,*}

^aInstitute of Medical Engineering, Graz University of Technology, Stremayrgasse 16/III, 8010 Graz, Austria

^bDepartment of Neurology, Division of General Neurology, Medical University of Graz, Auenbruggerplatz 22, 8036 Graz, Austria

^cDivision of Neuroradiology, Vascular and Interventional Radiology, Department of Radiology, Medical University of Graz, Auenbruggerplatz 22, 8036 Graz, Austria

^dInstitute of Biomedical Informatics, Graz University of Technology, Stremayrgasse 16/I, 8010 Graz, Austria

^eBioTechMed-Graz, Mozartgasse 12/II, 8010 Graz, Austria

^fApplication Development, Siemens Healthcare, Henkestraße 127, 91052 Erlangen, Germany

^gInstitute of Mathematics and Scientific Computing, University of Graz, Heinrichstraße 36, 8010 Graz, Austria

ARTICLE INFO

Article history:

Received 2020

Received in final form xxxx

Accepted xxxx

Available online xxxx

Communicated by NN

2010 MSC: 92C55, 68U10, 94A12

Keywords: quantitative ASL, non-linear fitting, quantitative mapping, stroke

ABSTRACT

Multi-Delay single-shot arterial spin labeling (ASL) imaging provides accurate cerebral blood flow (CBF) and, in addition, arterial transit time (ATT) maps but the inherent low SNR can be challenging. Especially standard fitting using non-linear least squares often fails in regions with poor SNR, resulting in noisy estimates of the quantitative maps. State-of-the-art fitting techniques improve the SNR by incorporating prior knowledge in the estimation process which typically leads to spatial blurring. To this end, we propose a new estimation method with a joint spatial total generalized variation regularization on CBF and ATT. This joint regularization approach utilizes shared spatial features across maps to enhance sharpness and simultaneously improves noise suppression in the final estimates. The proposed method is evaluated at three levels, first on synthetic phantom data including pathologies, followed by in vivo acquisitions of healthy volunteers, and finally on patient data following an ischemic stroke. The quantitative estimates are compared to two reference methods, non-linear least squares fitting and a state-of-the-art ASL quantification algorithm based on Bayesian inference. The proposed joint regularization approach outperforms the reference implementations, substantially increasing the SNR in CBF and ATT while maintaining sharpness and quantitative accuracy in the estimates.

© 2021 Elsevier B. V. All rights reserved.

1. Introduction

Arterial spin labeling (ASL) is a non-invasive MRI technique for quantifying local tissue perfusion (Detre et al., 1992). The method utilizes magnetically labeled blood water by invert-

*Corresponding author:

Tel.: +43-316-873-35401; fax: +43-316-873-1035400;

e-mail: oliver.maier@tugraz.at (Oliver Maier),

stefan.spann@tugraz.at (Stefan M Spann),

daniela.pinter@medunigraz.at (Daniela Pinter),

thomas.gattringer@medunigraz.at (Thomas Gattringer),

nicole.hinterregger@medunigraz.at (Nicole Hinteregger),

gerhard.thallinger@tugraz.at (Gerhard G. Thallinger),

chris.enzinger@medunigraz.at (Christian Enzinger),

josef.pfeuffer@siemens-healthineers.com (Josef Pfeuffer),

kristian.bredies@uni-graz.at (Kristian Bredies),

rudolf.stollberger@tugraz.at (Rudolf Stollberger)

ing the blood water spins upstream the imaging region. After waiting a specific period of time, called the post labeling delay (PLD) which accounts for the time the magnetically labeled blood needs to flow into the region of interest, an image is acquired. This so called label image is subtracted from a second image, the control image, acquired without magnetization alterations of the inflowing blood. From this difference image, also known as perfusion weighted image (PWI), the cerebral blood flow (CBF) can be quantified using a general kinetic model (Buxton *et al.*, 1998). The recommended clinical ASL protocol (Alsop *et al.*, 2014; Telischak *et al.*, 2014) consists of single-delay pseudo-continuous ASL (pCASL) (Dai *et al.*, 2008) combined with segmented 3D data acquisitions such as gradient and spin echo (GRASE) (Feinberg *et al.*, 2009; Günther *et al.*, 2005) or turbo spin echo (TSE) stack of spirals (SoSP) (Ye *et al.*, 2000; Dai *et al.*, 2008) readout due to efficient background suppression (Ye *et al.*, 2000) and SNR gains (Alsop *et al.*, 2014) of these methods. For single-delay acquisitions the signal in the PWI depends on both, the CBF and arterial transit time (ATT). Hence, the accuracy of CBF estimation from single-PLD ASL data is dependent on both factors. Another limitation is that for cases with prolonged ATT ($ATT > PLD$) some of the labeled blood may remain in larger vessels. This leads to bright spots and an overestimation in CBF in bigger vessels and an underestimation of CBF in brain areas. The bright spots are known as vascular artifacts and can complicate clinical diagnosis in patients with stroke, steno-occlusions, or moya-mayo disease (Zaharchuk, 2012). A way to improve the clinical interpretation of single-delay ASL images is by applying additional coefficient of variation maps obtained from the multiple PWIs (Mutsaerts *et al.*, 2017). Another way to reduce misquantification is by using a longer PLD, ensuring that the blood has sufficient time to reach the tissue. However, this leads to longer acquisitions and additionally to a lower SNR due to the T1-relaxation of the labeled blood. Alternatively, multi-PLDs can be used to sample the inflowing blood at several time points, from a short PLD to long PLD. By fitting the acquired signal to a kinetic model, the potential bias in CBF

due to unknown ATT can be reduced (Buxton *et al.*, 1998). In addition, this approach provides another important parameter, the ATT, which is helpful in characterization or detection of cerebrovascular diseases (Alsop *et al.*, 2014; MacIntosh *et al.*, 2010, 2014; Zaharchuk *et al.*, 2009; Zaharchuk, 2012). However, the recommended segmented acquisitions have the drawback of a low temporal resolution with increased sensitivity to inter-segment motion. Therefore, only a limited number of PLDs can be acquired in a clinically acceptable time. Recently, accelerated single-shot 3D acquisition strategies (Ivanov *et al.*, 2017; Boland *et al.*, 2018; Spann *et al.*, 2019) were implemented to overcome this drawback, at the cost of reduced SNR. This makes the estimation of reasonable quantitative ATT and CBF maps from this low SNR perfusion weighted time series challenging. The standard voxel-wise non-linear least squares (NLLS) fitting approach leads to outliers in low-SNR voxels. To this end, a weighted delay approach (Dai *et al.*, 2011) was proposed to reduce outliers in the quantitative maps. Further improvements could be achieved by inclusion of spatial priors on the CBF map (Groves *et al.*, 2009) in a Bayesian inference model (BASIL (Chappell *et al.*, 2010)). This stabilizes the fitting approach and reduces noise, ultimately leading to improved CBF estimates but introduces spatial blurring. Exploiting all available spatial information by means of joining the individual regularization of each unknown into a single, joint regularization functional can further improve reconstruction quality. Such an approach has been successfully applied in the context of relaxometry (Knoll *et al.*, 2017; Wang *et al.*, 2017; Maier *et al.*, 2018). Joint regularization utilizes information present in each map, such as tissue boundaries, by means of advanced spatial regularization functionals to avoid the loss of small features and promotes overall sharper parameter maps. In this study, we propose a new non-linear fitting algorithm with joint spatial constraints on the CBF and ATT map to stabilize the estimation procedure and hence enhance the image quality. To improve the motion robustness of the 3D acquisition, we combine the proposed method with a single shot CAIPIRINHA accelerated 3D GRASE readout. The method is evaluated on synthetic phan-

tom datasets including simulated pathologies, on six healthy subjects, as well as on seven stroke patients and compared to NLLS and BASIL without regularization on ATT (*BASIL w/o*) and with regularization on CBF and ATT (*BASIL w/*).

2. Theory

2.1. Fixing notation

Throughout the work we fix the following notations. The image dimensions in 3D are denoted as N_i, N_j, N_k , defining the image space $U = \mathbb{R}^{N_i \times N_j \times N_k}$ with $x = (i, j, k)$ defining a point at location $(i, j, k) \in \mathbb{N}^3$. $u \in U^{N_u}$ expresses the space of unknown CBF- and ATT-maps with $N_u = 2$ in this case. The measured data space is denoted as $D = \mathbb{C}^{N_i \times N_j \times N_k}$ and consists of N_d perfusion weighted images derived from Control/Label (C/L)-pairs, measured at time $t = (t_1, t_2, \dots, t_{N_d}) \in \mathbb{R}_+^{N_d}$.

2.2. Parameter fitting

From a statistical point of view the problem of identifying the unknown parameters $u = (u_1, u_2, \dots, u_{N_u}) \in U^{N_u}$ given a series of noisy measurements $d = (d_1, d_2, \dots, d_{N_d}) \in D^{N_d}$ can be solved via maximum likelihood estimation. Assuming the measurements at time t_n are generated by some function $A_{\phi, t_n} : u \mapsto d_n$ with fixed parameters ϕ the likelihood function of measuring d is given by $p(d|u, A_{\phi, t_n})$. The realization of p depends on the noise distribution in the measurements d . Under the assumption that additive independent and identically distributed zero-mean Gaussian noise with variance σ^2 (AWGN) corrupts the measurements d , the multivariate likelihood function turns into a product of single-variate functions. It is common to minimize the negative logarithm of the likelihood function, which is equivalent to maximizing the likelihood, as it turns the product into a sum and improves the numerical stability. Omitting constant terms with respect to u yields

$$u^* \in \arg \min_{u \in U^{N_u}} \frac{1}{2\sigma^2} \sum_{n=1}^{N_d} \|A_{\phi, t_n}(u) - d_n\|_2^2 \quad (1)$$

which resembles the well known minimum least squares problem with $\|\cdot\|_2$ being the standard L^2 -norm.

Typically, several measurements with varying sequence parameters are necessary to quantify tissue parameters. Especially in cases with a non-linear relationship between acquired signal and parameters, fitting is performed in an iterative fashion.

2.3. The ASL signal model

The quantification of CBF and ATT is based on the standard model for pseudo-continuous ASL (pCASL) (Buxton *et al.*, 1998) which reads as

$$A(u)_{\phi, t_n} = \begin{cases} 0, & t_n < \Delta \\ 2M_{0\alpha} f T_1 e^{-\frac{\Delta}{T_{1b}}} \left(1 - e^{-\frac{t_n + \tau}{T_{1app}}}\right), & \Delta \leq t_n < \Delta + \tau \\ 2M_{0\alpha} f T_1 e^{-\frac{\Delta}{T_{1b}} - \frac{t_n - \tau - \Delta}{T_{1app}}} \left(1 - e^{-\frac{\tau}{T_{1app}}}\right), & \Delta + \tau \leq t_n \end{cases} \quad (2)$$

where $u = (f, \Delta)$ and f amounts to CBF in ml/g/s, but is normally quoted in ml/100g/min, and Δ to ATT in seconds. The a priori known parameters of equation 2 are combined into the variable $\phi = (M_{0\alpha}, T_1, T_{1b}, \tau)$. It is assumed that T_1 , the apparent longitudinal relaxation decay constant of the tissue, amounts to 1.33 seconds at 3T. T_{1b} is the longitudinal relaxation decay constant of blood, assumed to amount to 1.65 seconds at 3T (Lu *et al.*, 2004). τ corresponds to the labeling duration, α is the labeling efficiency and set to 0.7 (Dai *et al.*, 2008) and t_n is the acquisition time point, i.e. the sum of post labeling delay and labeling duration, for the n^{th} measurement. Further, the blood-brain partition coefficient λ is assumed to be 0.9 ml/g (Herscovitch and Raichle, 1985) thus $1/T_{1app}(f) = 1/T_1 + f/\lambda$, and $M_{0\alpha} = \alpha M_0/\lambda$ with M_0 being the acquired proton density weighted image.

2.4. Regularization

As the acquired PWI images suffer from poor SNR the problem of quantifying CBF and ATT typically suffers from numerical instabilities. A method to incorporate a priori knowledge of the parameters u into the maximum likelihood estimation problem 1 is known as maximum a posteriori estimation and leads to

$$\min_u \frac{1}{2} \sum_{n=1}^{N_d} \|A_{\phi, t_n}(u) - d_n\|_2^2 + \gamma R(u), \quad (3)$$

with $\gamma > 0$ balancing between the data fidelity term and the regularization R . $R(u)$ includes known information about u such as its statistical distribution or spatial features, e.g. u should consist of piece-wise constant areas. As the variance σ^2 is in general unknown, we will not consider σ^2 fixed but as something that can be chosen in the reconstruction process. Thus, we combine it with the regularization parameter γ . The introduced prior can lead to a biased estimate of u with reduced uncertainties (Brinkmann *et al.*, 2017). Thus a trade-off between faithfulness to acquired data and the prior needs to be determined according to the expected noise in the data. The most basic form consists of classical Tikhonov regularization which penalizes outliers in the parameter maps in an L^2 -norm sense (Tikhonov and Arsenin, 1977). An extension to this basic form consists of penalizing the gradient of the maps which is known as H^1 regularization (Tikhonov and Arsenin, 1977), leading to a smoother appearance but comes at the cost of blurred edges. To preserve edges and to obtain a better visual impression, a sparsity promoting functional is usually preferred which can be realized by posing an L^1 -norm based constraint on the sparse domain of the unknowns (Donoho, 2006; Lustig *et al.*, 2007). As u is usually not sparse in its native domain, a sparsifying transform such as a finite differences operation or a wavelet transformation is used. The total variation (TV) functional of Rudin-Osher-Fatemi (ROF) (Rudin *et al.*, 1992) is based on an L^1 -norm combined with a forward finite differences operator. This combination can be interpreted as a spatial piece-wise constant prior which is known to be prone to stair-casing artifacts in the final reconstruction results (Bredies *et al.*, 2010). In order to avoid these stair-casing artifacts but leverage the edge-preserving feature of TV a generalization termed total generalized variation (TGV) functional was proposed by Bredies *et al.* (2010). In the context of MRI, TGV^2 , which enforces piece-wise linear solutions by balancing between a first order and approximated second order derivative, was shown to yield excellent reconstruction results, preserving fine details and edges while maintaining the denoising properties of TV (Knoll *et al.*, 2010). In the discretized form the TGV^2 regularization is realized via a

minimization problem of the following form

$$TGV^2(u) := \min_v \beta_0 \|\nabla u - v\|_{1,2} + \beta_1 \|\mathcal{E}v\|_{1,2}. \quad (4)$$

The favorable properties of TGV^2 can be further improved by sharing common feature information between the unknown parameter maps by joining the TGV^2 functionals utilizing a Frobenius norm in parametric dimension (Bredies, 2014). Recently, this combination was shown to yield improved reconstruction results compared to separate regularization on each map in the context of quantitative T_1 mapping (Maier *et al.*, 2018) and multi modal image reconstruction (Knoll *et al.*, 2017). The combination by means of a Frobenius norm is justified by the assumption that quantitative maps share the same features at the same spatial positions. To incorporate the Frobenius norm the following adaptations to the TGV^2 semi-norm definitions are made

$$\|v\|_{1,2,F} = \sum_{i,j,k} \sqrt{\sum_{l=1}^{N_u} |v_{i,j,k}^{1,l}|^2 + |v_{i,j,k}^{2,l}|^2 + |v_{i,j,k}^{3,l}|^2} \quad (5)$$

with $v = (v^{1,l}, v^{2,l}, v^{3,l})_{l=1}^{N_u} \in U^{3 \times N_u}$ constituting the approximation of 3D spatial derivatives, and for the symmetrized gradient $\chi = (\chi^{1,l}, \chi^{2,l}, \chi^{3,l}, \chi^{4,l}, \chi^{5,l}, \chi^{6,l})_{l=1}^{N_u} \in U^{6 \times N_u}$

$$\|\chi\|_{1,2,F} = \sum_{i,j,k} \sqrt{\sum_{l=1}^{N_u} |\chi_{i,j,k}^{1,l}|^2 + |\chi_{i,j,k}^{2,l}|^2 + |\chi_{i,j,k}^{3,l}|^2 + 2|\chi_{i,j,k}^{4,l}|^2 + 2|\chi_{i,j,k}^{5,l}|^2 + 2|\chi_{i,j,k}^{6,l}|^2} \quad (6)$$

2.5. The non-linear, non-smooth optimization problem

The combination of TGV^2 with equation 3 leads to

$$\min_{u,v} \frac{1}{2} \sum_{n=1}^{N_d} \|A_{\phi, t_n}(u) - d_n\|_2^2 + \gamma(\beta_0 \|\nabla u - v\|_{1,2,F} + \beta_1 \|\mathcal{E}v\|_{1,2,F}) \quad (7)$$

which is a non-linear problem in the unknowns u and non-smooth due to the L^1 -norms of the TGV^2 functional. Recall that for the ASL signal, the non-linear operator $A_{\phi, t_n}(u)$ is defined by equation 2 and u amounts to $u = (f, \Delta)$. A similar problem arises in model-based quantification of T_1 and M_0 (Roeloffs

et al., 2016; Wang et al., 2017; Maier et al., 2018). The problem is thus solved in analogy via a two-step procedure. First the data fidelity term is linearized in a Gauss-Newton (GN) fashion, second the linearized, non-smooth sub-problem is solved using a primal-dual splitting algorithm. The linearized sub-problem for each linearization step k is given by

$$\begin{aligned} \min_{u,v} \quad & \frac{1}{2} \sum_{n=1}^{N_d} \|DA_{\phi,t_n}|_{u=u^k} u - \tilde{d}_n^k\|_2^2 + \\ & \gamma_k (\beta_0 \|\nabla u - v\|_{1,2,F} + \beta_1 \|\mathcal{E}v\|_{1,2,F}) + \\ & \frac{\delta_k}{2} \|u - u^k\|_{M_k}^2, \end{aligned} \quad (8)$$

Constant terms stemming from the linearization at position u^k are fused with the data by $\tilde{d}_n^k = d_n - A_{\phi,t_n}(u^k) + DA_{\phi,t_n} u^k$ and the matrix $DA_{\phi,t_n}|_{u=u^k} = \frac{\partial A_{\phi,t_n}}{\partial u}(u^k)$, i.e. the derivative of the signal with respect to each unknown, can be precomputed in each linearization step. The additional weighted L^2 -norm penalty $\|u - u^k\|_{M_k}^2 = \|M_k^{\frac{1}{2}}(u - u^k)\|_2^2$ improves convexity of the function and resembles a Levenberg-Marquadt update if the weight matrix M is chosen as $M_k = \text{diag}(DA_{\phi,t_n}|_{u=u^k}^T DA_{\phi,t_n}|_{u=u^k})$ or a simpler Levenberg update if M_k is chosen as identity matrix. It was shown by Salzo and Villa (2012) that the GN approach converges with linear rate to a critical point for non-convex problems with non-differential penalty functions if the initialization is sufficiently close. By exploiting the Fenchel duality it is possible to transform the problem in equation 8 into a saddle-point form

$$\min_u \max_y \langle Ku, y \rangle + G(u) - F^*(y), \quad (9)$$

which overcomes the non-differentiability issue of the L^1 -terms. Problems of the form in (9) can be efficiently solved using a first order primal-dual splitting algorithm (Chambolle and Pock, 2010) in combination with a line search (Malitsky and Pock, 2018) to improve the convergence speed. The detailed derivation is given in the Appendix A. Pseudo-code for the implementation can be found in Appendix B.

2.6. Reference Methods

For comparison of the proposed algorithm we used the non-linear least squares (NLLS) as well as the Bayesian Inference

for Arterial Spin Labeling MRI (BASIL) method (Chappell et al., 2009; Groves et al., 2009). The NLLS method solves equation 1 without regularization by means of a trust-region reflective method implemented by *lsqnonlin* in MATLAB (The Mathworks, Natick, MA, USA). This method uses additional box constraints on CBF and ATT to limit their values to a physiologically meaningful range of [0, 300] ml/100g/min for CBF and [0, 6] seconds for ATT respectively. BASIL is included in FSL (Smith et al., 2004; Woolrich et al., 2009; Jenkinson et al., 2012) and uses Bayesian inference to estimate the unknown parameter maps. It incorporates fixed non-spatial priors as well as adaptive non-local spatial smoothing priors for the parameters. The spatial smoothing prior is used for CBF and is directly based on evidence in the data. The smoothing strength is adjusted based on the local support in the specific area in the data. The arterial (macro-vascular) contribution flag was set to "OFF" in BASIL to facilitate comparability to the proposed method which currently implements the pCASL model omitting the local arterial contribution. In addition to this standard form of BASIL, termed *BASIL w/o*, a simple duplication of the line associated with spatial priors in the starting script enables priors on both, CBF and ATT, as described in (Chappell et al., 2009; Groves et al., 2009). This modification serves as second BASIL reference and is termed *BASIL w/*.

3. Methods

3.1. Synthetic ASL data

3.1.1. Phantom generation

To evaluate the proposed method, synthetic ASL data was generated from brain T_1 and PD maps supplied by MRiLab (Liu et al., 2017) for MATLAB with a matrix size of $216 \times 180 \times 180$ and 1 mm³ isotropic resolution. Gray (GM) and white matter (WM) CBF values of 65 ml/100g/min and 20 ml/100g/min as well as ATT values of 0.8 s and 1.5 s, reported for the healthy human brain were assigned to the tissue maps. In a subsequent step the quantitative maps were down sampled onto a $72 \times 60 \times 60$ grid, matching typical matrix sizes and resolution (3 mm³ isotropic) of 3D ASL acquisitions. A small linear

phase variation of -0.5 to 0.5 rad going from anterior to posterior was added to the M_0 image to obtain a complex valued image. The signal equation (2) was used to generate a series of PWI images. The control images $C \in D^{N_d}$ were assumed to correspond to $C = (1 - \alpha)M_0$, which models the background suppression applied to M_0 . The label images $L \in D^{N_d}$ were simply given by $L = C - \text{PWI}$. 3-D coil sensitivity profiles were computed using Biot-Savart's law. The 20 coils were placed equally spaced on a spherical surface. The coil sensitivity maps were multiplied with the complex control- and label-images. The resulting weighted images were then transformed into k-space via Fourier transformation and zero mean complex Gaussian noise was added to each k-space. The standard deviation of the added Gaussian noise was 0.65 which results approximately in an SNR of 4 in WM and 6 in GM (assuming a LD of 1.8s and a PLD of 1.75s). Noisy complex control and label images were then computed using a phase sensitive reconstruction based on Roemer *et al.* (1990), using the complex conjugate coil images. The noisy control and label pairs constituted the final PWI sequence. For our approach the complex valued PWIs were used as input for the fitting process. For BASIL, the PWIs were calculated by subtracting the absolute valued label image from the control image as BASIL does not support complex valued images. In total $N_d = 32$ time points in two series, each containing 16 time points, were simulated with the parameters of the ASL model amounting to $\lambda = 0.9$, $T_{1b} = 1650$ ms, $\tau = (1050, 1300, 1550, 1800, \dots, 1800)$ ms, $t = (1050 : 250 : 4800)$ ms, $\alpha = 0.7$. M_0 and T_1 amounted to the down sampled values supplied by the MRiLab phantom. In addition to the healthy brain phantoms of MRiLab we simulated perfusion changes in GM and WM. In total, six cases, denoted by Case 1 to Case 6, were generated. It should be noted that all pathologies were drawn in the high-resolution space to get smoother transitions in the ASL space. For Case 1 to Case 3 the following pathologies in a region in frontal WM and in a part of the putamen (GM) were simulated as illustrated in Figure 1:

Case 1: No changes to values, i.e. healthy.

Case 2: Hyperperfusion of 113.75 ml/100g/min in GM and 50

ml/100g/min in WM without changes in corresponding areas in ATT.

Case 3: Hyperperfusion of 113.75 ml/100g/min in GM and 40 ml/100g/min in WM with corresponding reduced arterial transit time of 0.4 s in GM and 0.75 s in WM.

In addition we simulated cases with normal CBF and increased ATT by a partly-blockage of the arteria cerebri media and a small region in the frontal lobe illustrated in Figure 2:

Case 4: Normal perfusion with increased ATT of 2.75 s.

Case 5: Normal perfusion with increased ATT of 3 s.

Case 6: Normal perfusion with increased ATT of 3.25 s.

To assess the influence of joint regularization the proposed method was run without regularization on ATT (*Proposed w/o*) by simply setting the finite differences based image gradient of ATT to zero in all iterations. The joint regularization was denoted as *Proposed w/*. The CBF and ATT estimates of the individual fitting algorithms were compared to each other based on visual inspection, pixel-wise absolute difference plots, and evaluation of median and inter quartile range (IQR) in the simulated ROIs, i.e. median and IQR of GM, WM, and each simulated lesion. In addition, 2D histograms of CBF and ATT for each method were generated by combining all simulated cases into one distribution of CBF and ATT, respectively.

3.1.2. Error propagation and stability

To assess the error propagation and stability due to the non-linear fitting procedure we performed a pseudo replica analysis for all three methods. To this end, 100 different noise realizations with a standard deviation of 0.65 were simulated for Case 3. Due to the non-linear fitting process a Gaussian noise assumption in the parameter maps could be violated, thus the median and inter-quartile range between the 25th and 75th quartile were used for evaluation. We assessed potential biases using the medians of differences to the ground truth of the 100 realisations and compared the differences in the IQRs between the methods. For the synthetic dataset GM and WM binary masks, generated on the ground truth phantom, are employed.

Based on the down sampled GM and WM mask, low resolution mask were generated by thresholding the corresponding GM/WM masks with 0.7. Mask for the simulated lesions were generated in analogy.

Additionally, we compared the estimated CBF and ATT maps of the proposed method with the results of BASIL and NLLS by means of a relative difference to the numerical ground truth parameter maps.

To assess if differences in median or IQR are statistically significant, we applied Mann-Whitney-U tests, as medians and IQR distributions may deviate from a normal distribution. The medians and IQRs were computed in ROIs for the 100 reported noise realizations. Medians were then compared to the median of the noise free reference. For the IQRs the proposed method was tested against the other methods to show if statistically significant differences were observable. p-values were adjusted for multiple comparisons using the method of Bonferroni (1936). Each method and tissue was considered as parallel test case. Median and IQR of CBF and ATT were considered as separate cases. Results were considered statistically significant for p-values less than 0.05 ($p < 0.05$).

3.2. *In vivo measurements*

All measurements were performed on a 3T MAGNETOM Prisma (Siemens Healthcare, Erlangen, Germany) system using a 20-channel head coil. Written informed consent was obtained by all healthy volunteers as well as by all patients following the local ethics committee's regulations. In total, six healthy volunteers, consisting of five male and one female subject with an age of 29.5 ± 2.6 years were analyzed. Additionally, seven patients with ischemic stroke due to middle cerebral artery occlusion who received successful re-canalization therapy (i.e. intravenous thrombolysis followed by mechanical thrombectomy), consisting of six male and one female subject with an age of 57.1 ± 13 years, were considered. Patient data was acquired 24 hours after recanalization therapy. ASL images were acquired using a prototype 3D pCASL sequence with a 2D CAIPIRINHA accelerated single-shot 3D GRASE readout (Ivanov *et al.*, 2017) and two background suppression pulses

(Vidorreta *et al.*, 2013). Labeling efficiency for this sequence was experimentally determined in Vidorreta *et al.* (2013) and assumed as $\alpha = 0.7$. The following image parameters were used: FOV = $192 \times 192 \times 114 \text{ mm}^3$, matrix = $64 \times 64 \times 38$ resulting in 3 mm^3 isotropic resolution, 10% phase and 17.5% slice oversampling, TR = 5260 ms, TE = 14.44 ms, $2 \times 2^{(1)}$ CAIPIRINHA scheme, phase-partial Fourier 6/8, refocusing FA = 180° , EPI-factor = 25, turbo-factor (TF) = 22, resulting in one segment. 16 time points were acquired with a labeling duration of $\tau = (1050, 1300, 1550, 1800, \dots, 1800)$ ms and a PLD of $(0, 0, 0, 0 : 250 : 3000)$ ms. The PLDs were acquired in sequential order and the sequence of PLDs was repeated four times. Additionally, one proton density weighted image was acquired for each healthy subject, resulting in an acquisition time of 11 min 29 s. Due to time restrictions only two averages per PLD were acquired for the patients (5 min 53 s). The ASL labeling plane was placed according to a time-of-flight angiography in the neck area above the bifurcation of the carotid artery.

Additionally, for each healthy subject a T_1 weighted image was acquired using a 3D-MPRAGE sequence with the following imaging parameters: 1 mm^3 isotropic resolution, 176 slices, TR = 1900 ms, TE = 2.7 ms, TI = 900 ms, flip angle = 9° , acquisition time = 5 min 58 s.

3.2.1. *ASL Data Processing*

The accelerated ASL images were reconstructed directly on the scanner console by means of a prototype reconstruction pipeline provided by the vendor. The reconstructed ASL images were motion corrected using Statistical Parameter Mapping (SPM)¹² (Wellcome Trust Centre for Neuroimaging, University College London, UK) (Friston *et al.*, 2007) and the ASL-Toolbox (Wang *et al.*, 2008; Wang, 2012). This rigid-body based motion correction process involved three sub-steps as described in Wang (2012). After reconstruction and motion correction the perfusion weighted time series were calculated. From this perfusion weighted time-series the CBF and ATT

¹²<https://www.fil.ion.ucl.ac.uk/spm/software/spm12/>

maps were estimated using the proposed method as well as the two reference methods. The fixed parameters ϕ amount to the same values as in the synthetic data set except for $T_1=1330$ ms, the approximate tissue T_1 relaxation constant.

3.2.2. Anatomical Image Processing

For each healthy subject brain masks and PV estimates for GM and WM were computed using FSL (FMRIB Software Library, Oxford, UK (Jenkinson *et al.*, 2012)) and BASIL. In a first step, non-brain tissue was removed from the high resolution structural (T_1 weighted) image using the FSL tool *BET* (Smith, 2002). In a second step, PV estimates for GM and WM were obtained from the T1w image using the FSL tool *FAST* (Zhang *et al.*, 2001). Third, the structural image and brain mask were registered to the mean ASL image using the FSL tool *FLIRT* with 6 degrees of freedom (Jenkinson and Smith, 2001; Jenkinson *et al.*, 2002). The obtained transformation matrix served as initial guess for the next registration refinement step, implemented in BASIL. This step used the *epi_reg* tool of FSL for boundary based registration of the perfusion image with the segmented white matter mask (Greve and Fischl, 2009). In the last step, the PV estimates for GM and WM were transformed to the ASL-space by a process that integrates over the volume of the low resolution voxels as described by Chappell *et al.* (2011) and implemented in the FSL tool *applywrap*. Finally GM and WM binary masks in ASL space were computed by thresholding the PV estimates at 70% in WM and GM respectively. For the patient data brain masks were generated from the M_0 image using the FSL tool *BET* due to the missing T_1 weighted image.

3.2.3. Method Comparison

Healthy subjects were compared based on visual inspection of ATT and CBF for 1 and 4 acquired averages. In addition, WM and GM masks were used to compute median and IQR which were visualized with box-plots. Statistically significant differences in median and IQR between methods were assessed using Mann-Whitney-U tests, similar to the ones in the numerical simulation. p-values were adjusted for multiple comparisons (Bonferroni, 1936). Results were considered statistically

significant for p-values less than 0.05 ($p < 0.05$).

Stroke patients are compared based on visual inspection only.

3.3. Parameter optimization

To identify a good set of model and regularization parameters a grid search was performed on the synthetic dataset and in vivo healthy subjects. The resulting regularization parameters amounted to $\gamma_{init} = 10^{-3}$ and $\delta_{init} = 1$ which were reduced by 0.5 and 0.1 respectively after each Gauss-Newton step down to $\gamma_{final} = 6.5 \cdot 10^{-6}$ and $\delta_{final} = 10^{-2}$. A reduction of regularization parameters was observed to be beneficial for overall convergence in IRGN methods (Bakushinsky and Kokurin, 2004; Kaltenbacher *et al.*, 2008; Kaltenbacher and Hofmann, 2010). Relative tolerance for convergence was set to 10^{-8} between consecutive evaluations of function value. Regarding the inner iterations, 50 were used in the initial Gauss-Newton step and the number was increased by a factor of two until the maximum allowed number of 1000 iterations is reached, i.e. $iter^k = \min\{50 * 2^k, 1000\}$. A total of ten Gauss-Newton steps were performed. The ratio of the model parameters $\beta_0/\beta_1 = 1/2$ of TGV^2 was chosen according to Knoll *et al.* (2010). For in vivo data, the TGV^2 related weight $\gamma_{final} = 3 \cdot 10^{-5}$ was used.

3.4. Implementation

The proposed method is implemented in Python 3.7 (Python Software Foundation, <https://www.python.org/>) with OpenCL (Stone *et al.*, 2010; Klöckner *et al.*, 2012) based on a recently proposed quantitative MRI framework (Maier *et al.*, 2018, 2019, 2020) which utilizes GPU acceleration. Evaluation was done using Python 3.7 with NumPy 1.17.4 and SciPy 1.3.2. Computations were performed on a GPU server running Ubuntu 18.04, equipped with four Nvidia Titan XP cards (Nvidia Corporation, Santa Clara, CA, USA) and an Intel Xeon Gold 6136 CPU (Intel Corporation, Santa Clara, CA, USA) running at 3 GHz with 503 GB of RAM. The fitting code is available at <https://github.com/IMTtugraz/PyQMRI> and exemplary data as well as the used configuration files for

the optimization can be downloaded from

<https://doi.org/10.5281/zenodo.4493854>.

Scripts to generate the figures of this paper are available at

<https://doi.org/10.5281/zenodo.4494236>.

4. Results

We compare the fitting quality of our proposed joint spatial TGV² regularization strategy to established quantification on the CBF- and ATT-maps at three levels: First, synthetic phantom simulations demonstrate the accuracy and precision of NLLS, BASIL, and the proposed fit by means of a comparison to the ground truth values. This is further supported by a pseudo replica method to evaluate noise propagation into the final results. Violin-plots show the median and IQR distributions of estimated quantitative values and statistical tests assess the significance of differences between the methods. Second, the fitting algorithms are applied to in vivo ASL data acquired from six healthy volunteers. Results are compared visually and quantitatively by means of box-plots. Third, quantification of CBF and ATT is performed in patients following a stroke.

4.1. Synthetic phantom simulations

All synthetic phantoms were simulated with the ground truth values of CBF and ATT given in the leftmost column in figures 1 and 2. Each row corresponds to a different realization of pathologies as previously described. Fits in the second column, representing NLLS, show the highest noise in both CBF and ATT. The spatial prior on CBF incorporated in BASIL is able to reduce outliers, especially in low signal areas such as WM tracts, as shown in the third and fourth row. The most efficient noise reduction in both, CBF and ATT, is achieved by the proposed joint regularization method *Proposed w/*, which delivers comparable quantitative maps to the numerical ground truth. This visual impression is confirmed by the relative pixel wise differences to the ground truth in figures 3 and 4. The lack of spatial information in the NLLS approach leads to strong variations of values in low signal areas, evident in the first column of figure 3. *BASIL w/o* is able to reduce these outliers, showing

overall smoother appearance of errors but also the highest deviation in median WM CBF (table 1). However, for the estimated ATT-map both methods show similar relative difference. Using spatial priors on CBF and ATT (*BASIL w/*) reduces this variations but also seems to introduce a slightly lower value in ATT (table 1). The proposed method without joint regularization (*Proposed w/o*) shows reduced noise in CBF but similar results in ATT as *BASIL w/o*. The highest reduction in noise in both maps could be achieved with joint regularization on CBF and ATT (*Proposed w/*). This visual impression is also supported by the median and IQR values, evaluated for each tissue and presented in table 1. All methods show a slight overestimation of median CBF in WM. Approaches using spatial prior show a slight underestimation of median GM CBF. Similar, median WM ATT is slightly underestimated by all methods and *BASIL w/* shows the strongest deviation. This deviation is also visually noticeable in figure 1. *BASIL w/* and *Proposed w/* are showing the highest reduction of IQR in CBF and ATT compared to NLLS. For small lesions (Case 2 and 3), regularized methods show slight deviations in the median but again lower IQR than NLLS. Of all regularized methods, the proposed joint regularization performs best in GM lesions for both cases and WM lesions in CBF and ATT (Case 3). WM lesions in CBF only (Case 2) show the least deviations with *BASIL w/o*. For lesions with a severe increase in ATT but no variation of CBF (Case 4-6), the proposed method shows overall the least deviations to median CBF and ATT in WM but starts to degenerate for Case 6. Other methods are not able to recover WM CBF at all (Case 4-6). In large GM lesions median CBF estimates of NLLS are closest to the reference followed by the proposed method, but NLLS show an up to three fold increase in IQRs. Small GM lesions show similar results with *BASIL w/o* being second closest to the reference, followed by the proposed method. ATT values are underestimated by all methods. *Proposed w/* showing the least deviations to WM ATT in the large effected area and second closest for GM with NLLS being closer to the true median in GM. Small stroke GM ATT shows the least deviations using NLLS, followed by methods that do not regularize ATT. The

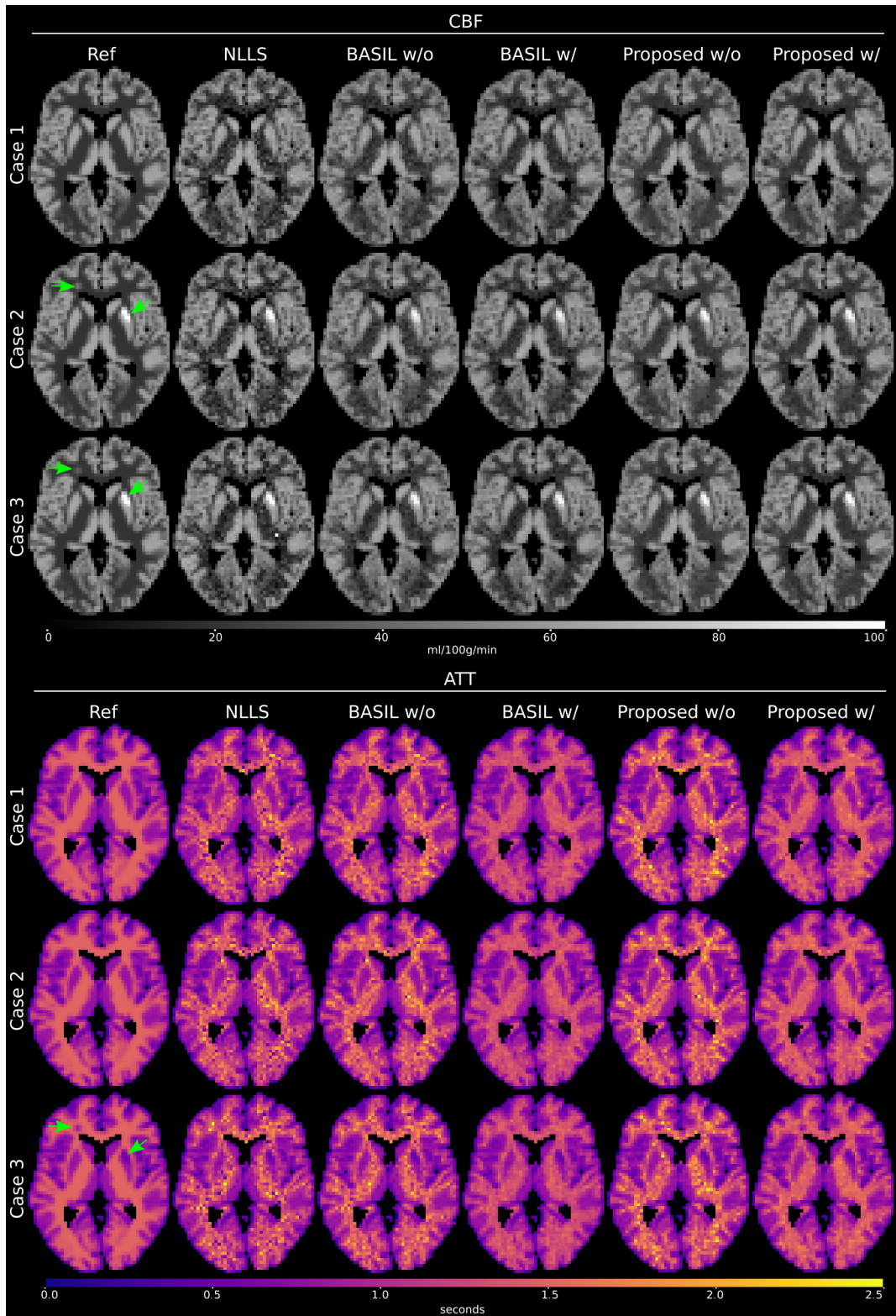


Fig. 1. CBF and ATT maps of synthetic phantoms for three different cases, one in each row (Case 1 - Case 3, top down). Case 1 has no simulated pathologies, Case 2 shows hyperperfusion in CBF only and Case 3 hyperperfusion in CBF and increased ATT in the corresponding area. In the first column the numerical ground truth is shown and in the following columns the estimated CBF- and ATT-maps from NLLS, BASIL without regularization on ATT (*BASIL w/o*), and with regularization on ATT (*BASIL w/*), and the proposed method without and with regularization on ATT, respectively. The proposed method with regularization on both unknown maps shows improved noise removal in CBF and ATT compared to the other methods due to joint spatial constraints. Median and 25% - 75% IQR for selected ROIs is given in table 1

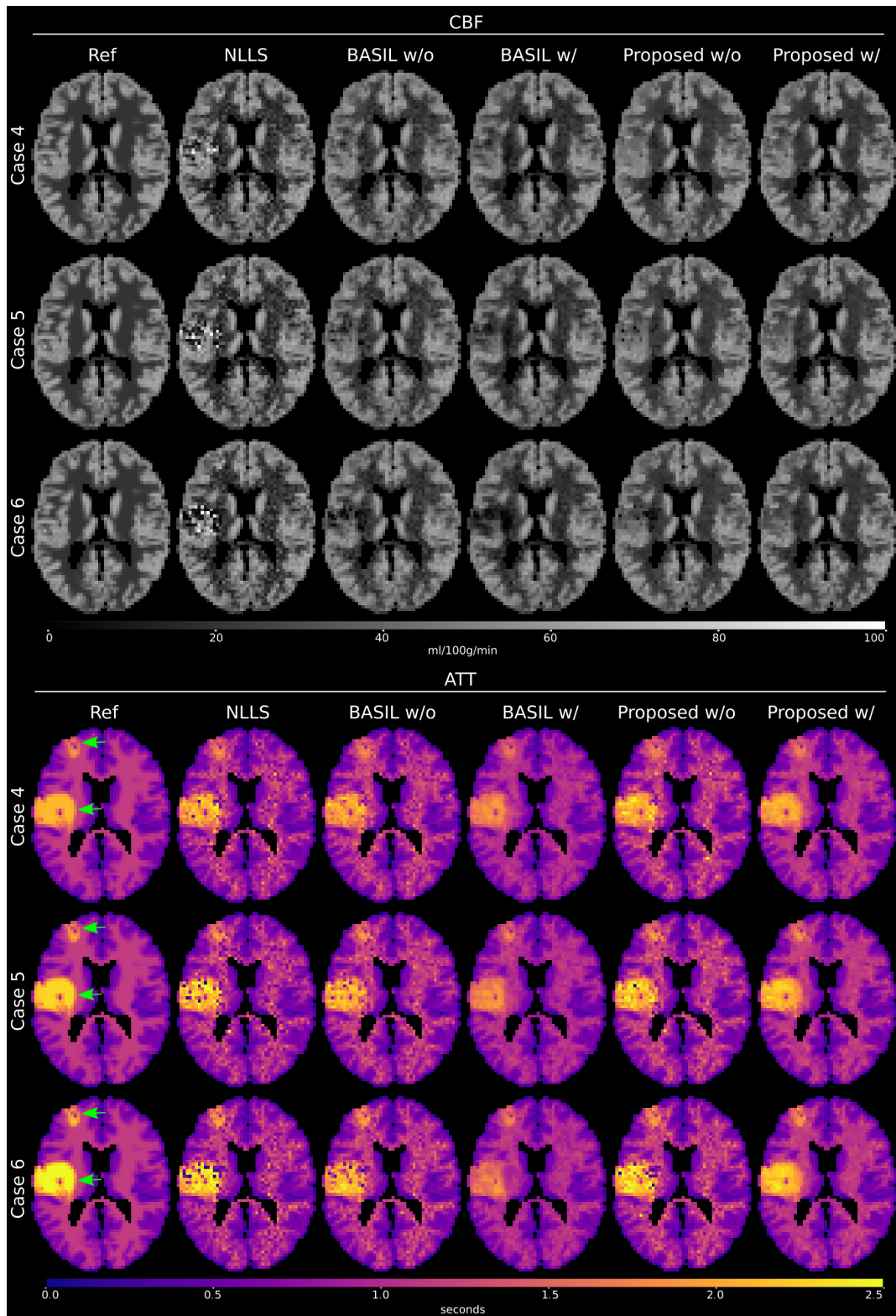


Fig. 2. CBF and ATT maps of synthetic phantoms of three cases with pathologies are shown. Each case represents a large partly occlusion of the arteria media combined with a small partly occlusion in frontal gray matter. No variation in CBF is simulated but each case shows an increase in ATT, which gets more severe from Case 4 to Case 6. The order of reference and displayed reconstruction algorithms is the same as in figure 1. The proposed method shows the least influence of the highly increased ATT on the CBF estimates and is able to recover higher ATT values in the affected areas than the other methods, as can be seen in table 1.

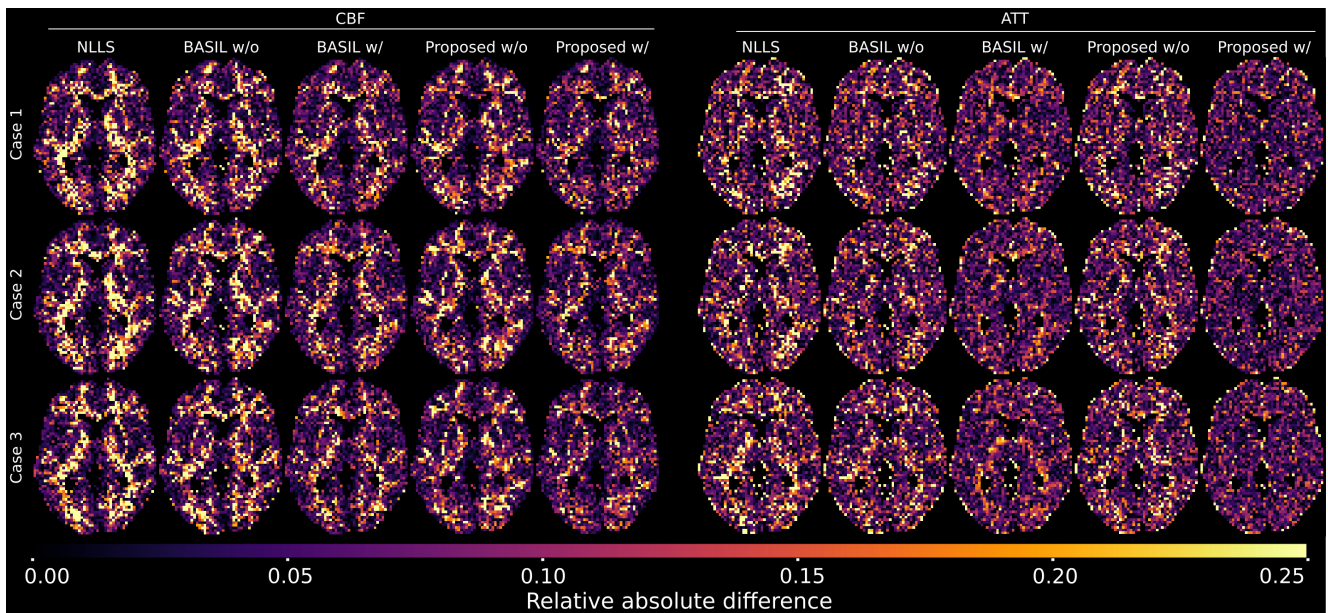


Fig. 3. Pixel-wise relative absolute difference between the ground truth numerical reference and the quantitative maps, estimated with the algorithms of figure 1. The NLLS shows the greatest deviation in ATT and CBF. *BASIL w/o* reduces the relative difference in the CBF due to the spatial prior and *BASIL w/* is able to reduce deviations even further. The *proposed w/o* method shows similar results on CBF and ATT as *BASIL w/o*. The least relative difference is achieved with the proposed method due to joint spatial constraints on CBF and ATT simultaneously.

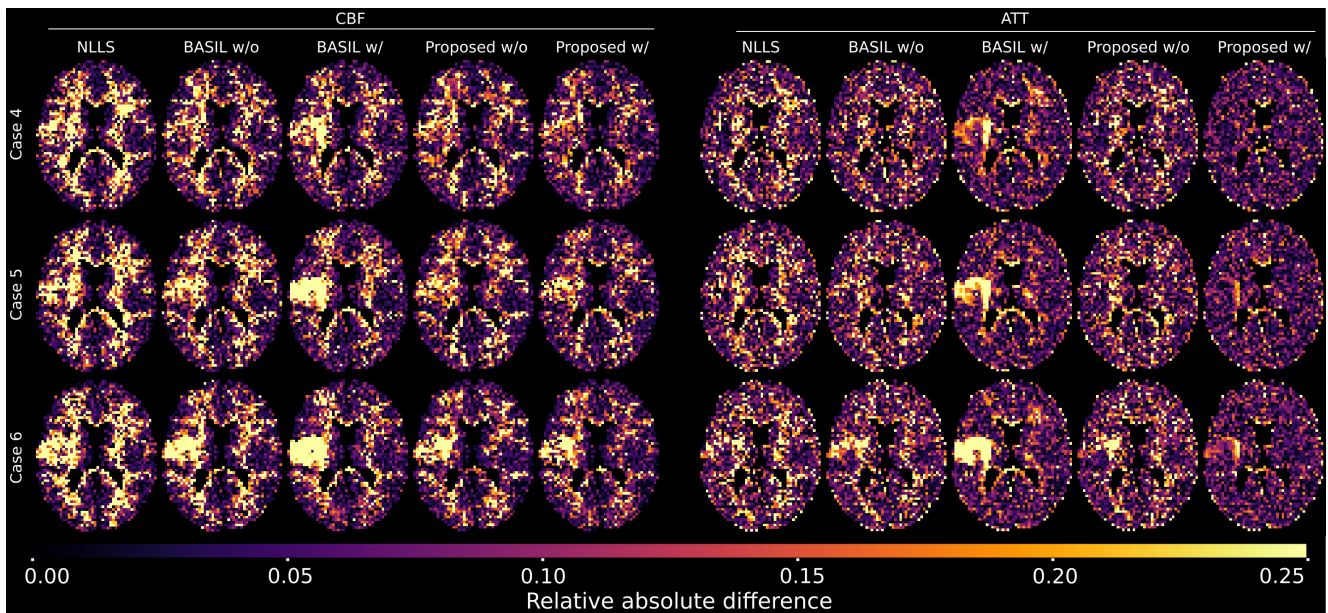


Fig. 4. Pixel-wise relative absolute difference between the ground truth numerical reference and the quantitative maps, estimated with the algorithms of figure 2. NLLS shows large deviation across the brain and in the simulated pathologies. *BASIL w/o* and *BASIL w/* can reduce this variation in normal appearing white and gray matter but variations in the large effected area remain. These variations are especially pronounced for *BASIL w/*. The proposed method is able to reduce variations in normal tissue and in addition shows smaller deviations in the pathological area, especially visible in ATT. Again, the proposed algorithm with regularization on CBF and ATT shows the least deviations overall.

Table 1. Median and (25%-75%) IQR for the simulated phantom data. Each ROI is based on the ground truth mask which was used for generating the lesion. w/o and w/ refers to regularization on CBF only and regularization on CBF and ATT, respectively. For cases 4-6, evaluation is performed only in the affected areas as normal appearing white and gray matter will be similar to cases 1-3. CBF values are given in ml/100g/min and ATT values in seconds.

Method	Ref	NLLS	BASIL w/o	BASIL w/	Proposed w/o	Proposed w/	
Tissue							
Case 1	WM CBF	21.79 (14.91-28.68)	23.72 (12.95-34.48)	25.74 (16.31-35.17)	23.29 (14.29-32.28)	25.68 (17.91-33.45)	24.16 (16.55-31.76)
	WM ATT	1.47 (1.36-1.58)	1.39 (1.06-1.72)	1.44 (1.14-1.74)	1.32 (1.17-1.48)	1.47 (1.16-1.78)	1.42 (1.26-1.58)
	GM CBF	57.12 (48.9-65.34)	57.24 (48.62-65.86)	55.81 (47.64-63.97)	55.31 (47.3-63.32)	55.74 (47.55-63.94)	55.83 (47.64-64.02)
	GM ATT	0.8 (0.66-0.94)	0.79 (0.64-0.95)	0.78 (0.63-0.93)	0.78 (0.63-0.93)	0.78 (0.63-0.93)	0.78 (0.63-0.93)
Case 2	WM lesion CBF	45.51 (42.89-48.13)	45.27 (36.04-54.49)	43.02 (37.76-48.28)	40.39 (36.64-44.19)	39.53 (34.06-45.0)	39.96 (36.42-43.5)
	WM lesion ATT	1.5 (1.5-1.5)	1.53 (1.46-1.61)	1.5 (1.39-1.61)	1.47 (1.4-1.53)	1.46 (1.35-1.57)	1.47 (1.41-1.54)
	GM lesion CBF	105.81 (97.02-114.59)	104.41 (92.69-116.13)	97.51 (88.41-106.62)	96.44 (86.8-106.08)	101.03 (89.51-112.55)	101.01 (89.5-112.52)
	GM lesion ATT	0.8 (0.8-0.8)	0.81 (0.77-0.85)	0.77 (0.73-0.81)	0.77 (0.73-0.8)	0.8 (0.76-0.83)	0.8 (0.76-0.83)
Case 3	WM lesion CBF	37.01 (35.26-38.75)	38.52 (35.95-41.08)	38.27 (36.39-40.14)	37.48 (34.34-40.61)	35.59 (33.95-37.24)	36.6 (35.26-37.94)
	WM lesion ATT	0.86 (0.8-0.93)	0.94 (0.77-1.11)	0.94 (0.74-1.14)	0.93 (0.77-1.08)	0.82 (0.67-0.97)	0.85 (0.7-1.0)
	GM lesion CBF	105.81 (97.02-114.59)	105.16 (93.12-117.21)	100.04 (89.28-110.8)	99.4 (88.66-110.15)	102.85 (92.81-112.89)	102.86 (92.88-112.85)
	GM lesion ATT	0.47 (0.39-0.54)	0.46 (0.4-0.52)	0.45 (0.37-0.52)	0.44 (0.38-0.51)	0.45 (0.39-0.52)	0.45 (0.38-0.52)
Case 4	Large Stroke WM CBF	20.12 (16.17-24.06)	14.0 (-6.07-34.07)	17.0 (3.08-30.92)	9.44 (-2.62-21.5)	20.42 (7.42-33.42)	22.23 (12.92-31.54)
	Large Stroke WM ATT	2.75 (2.73-2.77)	2.3 (1.0-3.6)	2.14 (1.31-2.96)	1.64 (1.03-2.26)	2.49 (1.64-3.35)	2.53 (2.24-2.83)
	Large Stroke GM CBF	55.33 (49.22-61.45)	54.18 (39.67-68.7)	47.26 (40.29-54.22)	42.01 (34.99-49.03)	47.67 (42.18-53.15)	47.73 (41.41-54.06)
	Large Stroke GM ATT	2.55 (2.18-2.92)	2.49 (2.05-2.92)	2.42 (2.07-2.76)	2.26 (1.98-2.54)	2.43 (2.07-2.79)	2.43 (2.14-2.72)
	Small stroke GM CBF	55.34 (48.07-62.6)	53.68 (42.47-64.89)	48.74 (41.27-56.2)	44.32 (39.14-49.5)	49.09 (42.37-55.81)	48.74 (42.63-54.85)
	Small stroke GM ATT	2.36 (2.05-2.68)	2.3 (1.97-2.64)	2.23 (1.96-2.5)	2.14 (1.93-2.35)	2.2 (1.95-2.45)	2.19 (1.99-2.4)
Case 5	Large Stroke WM CBF	20.12 (16.17-24.06)	9.81 (-8.44-28.07)	11.68 (-1.73-25.09)	5.9 (-3.41-15.2)	15.33 (-0.65-31.32)	20.52 (9.32-31.72)
	Large Stroke WM ATT	3.0 (2.97-3.03)	2.3 (0.58-4.02)	1.95 (0.99-2.9)	1.44 (0.7-2.18)	2.42 (1.14-3.71)	2.63 (2.24-3.01)
	Large Stroke GM CBF	55.33 (49.22-61.45)	54.23 (36.09-72.38)	44.28 (36.49-52.07)	36.41 (27.34-45.48)	45.33 (39.62-51.04)	45.75 (38.77-52.73)
	Large Stroke GM ATT	2.78 (2.37-3.19)	2.7 (2.22-3.18)	2.59 (2.23-2.95)	2.33 (2.05-2.6)	2.62 (2.26-2.98)	2.62 (2.32-2.91)
	Small stroke GM CBF	55.34 (48.07-62.6)	52.17 (37.33-67.02)	47.94 (43.06-52.82)	41.07 (36.81-45.32)	46.48 (41.25-51.71)	46.74 (42.03-51.45)
	Small stroke GM ATT	2.56 (2.21-2.92)	2.48 (2.08-2.87)	2.37 (1.98-2.77)	2.22 (2.02-2.43)	2.39 (2.0-2.78)	2.35 (2.03-2.67)
Case 6	Large Stroke WM CBF	20.12 (16.17-24.06)	6.88 (-5.98-19.75)	6.91 (-2.88-16.7)	2.92 (-3.16-8.99)	8.37 (-2.31-19.05)	15.68 (3.77-27.6)
	Large Stroke WM ATT	3.25 (3.22-3.28)	2.25 (0.23-4.27)	1.68 (0.79-2.56)	1.17 (0.55-1.78)	2.17 (0.29-4.05)	2.57 (2.11-3.03)
	Large Stroke GM CBF	55.33 (49.22-61.45)	50.61 (25.83-75.39)	37.62 (27.57-47.67)	26.08 (14.71-37.45)	41.21 (33.75-48.67)	40.37 (32.33-48.42)
	Large Stroke GM ATT	3.01 (2.56-3.46)	2.81 (2.31-3.3)	2.69 (2.35-3.03)	2.22 (1.9-2.53)	2.72 (2.35-3.1)	2.75 (2.47-3.02)
	Small stroke GM CBF	55.34 (48.07-62.6)	51.99 (31.45-72.53)	45.59 (39.66-51.52)	38.03 (29.86-46.21)	42.97 (37.43-48.5)	43.27 (36.83-49.71)
	Small stroke GM ATT	2.76 (2.38-3.14)	2.5 (2.05-2.95)	2.51 (2.23-2.79)	2.27 (2.07-2.47)	2.46 (2.18-2.74)	2.42 (2.23-2.62)

differences to the reference method are visualized by means of 2D histograms in figure 5. These histograms combine pixels of all six cases into one CBF and ATT plot per method. As seen in the pixel-wise difference maps in figure 3 and figure 4, all regularized methods show a slight tendency to overestimate low CBF values and underestimate high CBF values but NLLS shows the highest deviations. *BASIL w/o* is able to reduce these variance in CBF but shows minor underestimation of high CBF values and more severe underestimation of high ATT values. *BASIL w/* shows even more underestimation of CBF and a pronounced underestimation of high ATT values. The proposed method w/o shows reduced variations in CBF and variations similar to NLLS in ATT. The least variations in CBF and ATT can be achieved with *Proposed w/*, showing a minor underestimation of high CBF and ATT values.

The voxel-wise stability of the fitting methods was assessed based on 100 different noise realizations of Case 3 of the phantom simulations. For the evaluation, medians and IQRs of the 100 runs were visualized and differences statistically analyzed. A qualitative comparison of the median values for CBF- and

ATT-maps shows a good agreement to the noise free numerical maps for all four methods (figure 6). However, median WM and GM differences to the ground truth of the four approaches are statistically different at a significance level of 0.05 (table 2). With the exception of both *BASIL* methods, deviations in the CBF WM lesion are also statistically significant. ATT deviations in the WM lesion are statistically significant for all methods. The CBF GM lesion also shows statistically significant differences to the reference in all methods. ATT deviations in the GM lesion are not statistically significant for NLLS. These differences to the median reference value are visualized by a violin plot in the left half of figure 7.

Variations of the reconstruction algorithms over the 100 runs are reflected by the IQR in each ROI. The median of these variations is plotted in the right half of figure 7. The IQRs are highest for NLLS, except for the CBF GM lesion where both *BASIL* approaches show higher fluctuations. The proposed method shows a lower median IQR in WM CBF which is also statistically significant lower compared to all other approaches (table 2). For WM ATT, similar results are obtained with the ex-

Table 2. Medians of 100 noise realizations of Case 3 for differences to reference and IQRs for both CBF and ATT based on four different tissue types: WM, GM, and lesions in WM and GM, respectively. Mann-Whitney-U-tests were performed to assess whether differences between approaches are statistically significant. p-values are corrected for multiple testing using the Bonferroni method. For each run of the 100 noise realizations the median is computed in a selected ROI and these 100 medians are compared to the reference median by means of a Mann-Whitney-U test. Similar, the IQR between 25 % and 75 % is computed in the same ROI and the different methods are compared to the proposed reconstruction.

Value	Tissue Comparison	WM		GM		WM lesion		GM lesion	
		median	adj. p-value	median	adj. p-value	median	adj. p-value	median	adj. p-value
Median diff. to Ref CBF in ml/100g/min	NLLS - Ref	1.88e+00	4.51e-38	9.43e-02	4.51e-38	7.96e-01	2.35e-04	-2.01e-01	2.05e-03
	BASIL w/o - Ref	3.93e+00	4.51e-38	-1.32e+00	4.51e-38	-2.51e-01	5.41e-01	-5.30e+00	4.51e-38
	BASIL w/ - Ref	1.46e+00	4.51e-38	-1.83e+00	4.51e-38	1.95e-01	1.00e+00	-6.04e+00	4.51e-38
	Prop - Ref	2.46e+00	4.51e-38	-1.33e+00	4.51e-38	-7.89e-01	5.59e-06	-3.26e+00	4.51e-38
Median diff. to Ref ATT in seconds	NLLS - Ref	-7.91e-02	4.51e-38	-5.79e-03	4.51e-38	-2.16e-02	2.35e-04	3.19e-03	2.94e-01
	BASIL w/o - Ref	-2.37e-02	4.51e-38	-1.61e-02	4.51e-38	-2.25e-02	2.93e-09	-1.79e-02	2.31e-28
	BASIL w/ - Ref	-1.43e-01	4.51e-38	-2.10e-02	4.51e-38	1.80e-02	2.35e-04	-2.09e-02	9.81e-34
	Prop - Ref	-3.86e-02	4.51e-38	-2.05e-02	4.51e-38	-9.07e-03	2.05e-03	-1.13e-02	4.95e-19
IQR CBF in ml/100g/min	Prop	7.83e+00		8.15e+00		4.58e+00		7.71e+00	
	Prop vs. NLLS	1.10e+01	3.07e-33	8.61e+00	3.07e-33	5.96e+00	1.38e-06	7.54e+00	1.00e+00
	Prop vs. BASIL w/o	9.75e+00	3.07e-33	8.12e+00	4.01e-04	4.43e+00	1.00e+00	9.37e+00	2.48e-08
	Prop vs. BASIL w/	9.21e+00	3.07e-33	8.03e+00	5.36e-28	4.00e+00	1.00e+00	9.26e+00	6.80e-08
IQR ATT in seconds	Prop	1.79e-01		1.48e-01		1.26e-01		6.69e-02	
	Prop vs. NLLS	3.33e-01	3.07e-33	1.53e-01	3.07e-33	1.58e-01	1.13e-04	6.72e-02	1.00e+00
	Prop vs. BASIL w/o	2.99e-01	3.07e-33	1.50e-01	3.04e-30	1.42e-01	8.36e-01	6.26e-02	4.69e-01
	Prop vs. BASIL w/	1.58e-01	3.07e-33	1.49e-01	5.62e-21	1.16e-01	1.00e+00	6.41e-02	9.30e-01

ception of *BASIL w/*, which shows lower IQR than the proposed method. In GM CBF, the proposed method shows statistically significantly lower IQR than NLLS but both *BASIL* approaches are able to further reduce IQR than the proposed method. IQR of GM ATT shows the least deviations in the proposed method. In the WM lesion the proposed method reduces IQR compared to NLLS in CBF and ATT statistically significant but no statistically significant difference to both *BASIL* methods is observed. The CBF GM lesion shows statistically significant reduction of IQR using the proposed method over *BASIL* but no difference to NLLS. In the corresponding ATT, no statistically significant differences of IQR are observable. All p-values and median IQRs are reported in table 2.

4.2. Healthy volunteers

Figure 8 and figure 9 illustrate three different exemplary slices of the estimated CBF- and ATT-maps for subject 3 in dependence of the numbers of averages. The remaining five healthy subjects are available as Supplementary Material Figures S1- S5. For four averages each method produces meaningful CBF- and ATT-maps. The influence of regularization becomes more pronounced if no averaging is performed, showing increased number of outliers in the NLLS fits. Both *BASIL* methods show a reduction in outliers in CBF and ATT. *BASIL*

Table 3. Statistical evaluation of median and IQR for the investigated methods. Displayed p-values are corrected for multiple testing using the Bonferroni method. For each subject the median is computed in a white and gray matter ROI and compared to the median of NLLS with 4 averages (NLLS-4) by means of a double-sided Mann-Whitney-U test, respectively. Similar, the IQR between 25% and 75% is computed in the same ROI and the different methods are compared to the proposed method.

Value	Tissue Comparison	WM		GM	
		median	adj. p-value	median	adj. p-value
Median CBF 4 aver	NLLS-4	3.03e+01		6.93e+01	
	NLLS-4 vs. BASIL w/o	3.12e+01	1	6.91e+01	1
	NLLS-4 vs. BASIL w/	2.71e+01	6.49e-01	6.85e+01	1
	NLLS-4 vs. Prop	2.92e+01	1	6.74e+01	1
Median CBF 1 aver	NLLS-4 vs. NLLS	3.00e+01	1	6.81e+01	1
	NLLS-4 vs. BASIL w/o	3.41e+01	1	6.72e+01	1
	NLLS-4 vs. BASIL w/	2.59e+01	5.77e-02	6.47e+01	1
	NLLS-4 vs. Prop	2.96e+01	1	6.60e+01	1
Median ATT 4 aver	NLLS-4	1.18e+00		1.15e+00	
	NLLS-4 vs. BASIL w/o	1.27e+00	1	1.17e+00	1
	NLLS-4 vs. BASIL w/	1.07e+00	1	1.13e+00	1
	NLLS-4 vs. Prop	1.19e+00	1	1.14e+00	1
Median ATT 1 aver	NLLS-4 vs. NLLS	1.07e+00	1	1.14e+00	1
	NLLS-4 vs. BASIL w/o	1.27e+00	1	1.17e+00	1
	NLLS-4 vs. BASIL w/	8.31e-01	3.55e-02	1.06e+00	1
	NLLS-4 vs. Prop	1.14e+00	1	1.14e+00	1
IQR CBF 4 aver	Prop	2.27e+01		2.41e+01	
	Prop vs. NLLS-1	2.25e+01	1	2.58e+01	1
	Prop vs. BASIL w/o	2.19e+01	1	2.46e+01	1
	Prop vs. BASIL w/	2.41e+01	1	2.60e+01	1
IQR CBF 1 aver	Prop	2.49e+01		2.55e+01	
	Prop vs. NLLS-1	2.74e+01	5.44e-01	2.84e+01	7.87e-01
	Prop vs. BASIL w/o	2.47e+01	1	2.31e+01	7.87e-01
	Prop vs. BASIL w/	2.60e+01	1	2.58e+01	1
IQR ATT 4 aver	Prop	7.36e-01		5.41e-01	
	Prop vs. NLLS-1	9.94e-01	6.09e-02	5.69e-01	1
	Prop vs. BASIL w/o	8.52e-01	1.57e-01	5.49e-01	1
	Prop vs. BASIL w/	5.84e-01	5.44e-01	5.39e-01	1
IQR ATT 1 aver	Prop	7.52e-01		5.76e-01	
	Prop vs. NLLS-1	1.12e+00	1.57e-01	6.34e-01	1
	Prop vs. BASIL w/o	7.87e-01	1	5.65e-01	1
	Prop vs. BASIL w/	5.16e-01	3.68e-01	5.32e-01	1

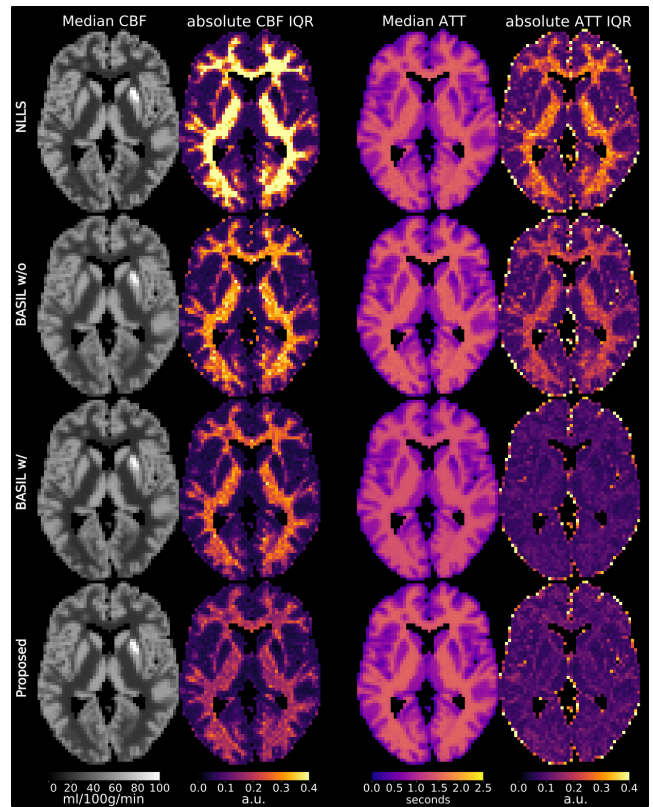
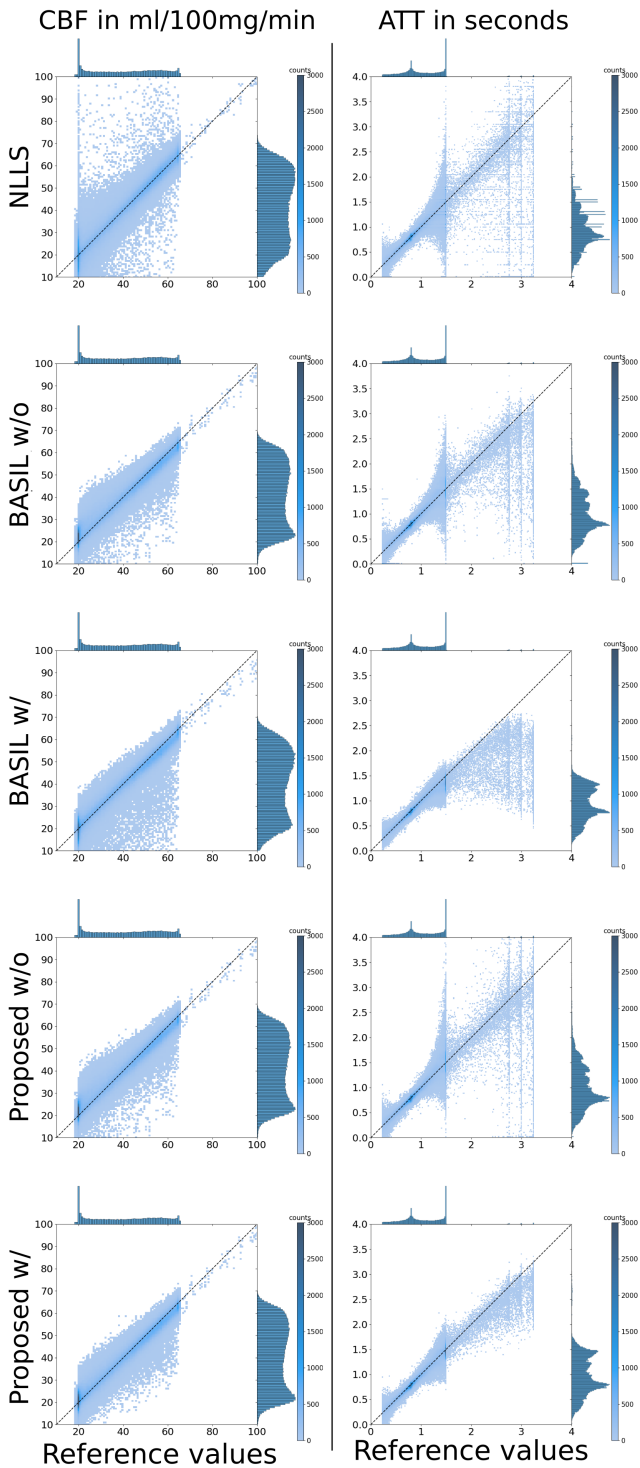


Fig. 6. Fitting results for the pseudo replica method of case 3, showing the median and 25%-75% IQR for the NLLS, *BASIL w/o*, *BASIL w/* and *Proposed w/* algorithm, respectively. 100 different noise realizations were used. For all four methods the median CBF- and ATT-maps are visually close to the noise free maps (figure 1). The IQR in CBF and ATT is lowest for the proposed method, showing the least fluctuations between individual runs.

Fig. 5. 2D histograms between reference values and fitted values for all methods. The dashed line represents identity. Points below correspond to underestimation and points above to overestimation compared to the reference value. Pixel values from all six cases are combined into one 2D histogram for each method.

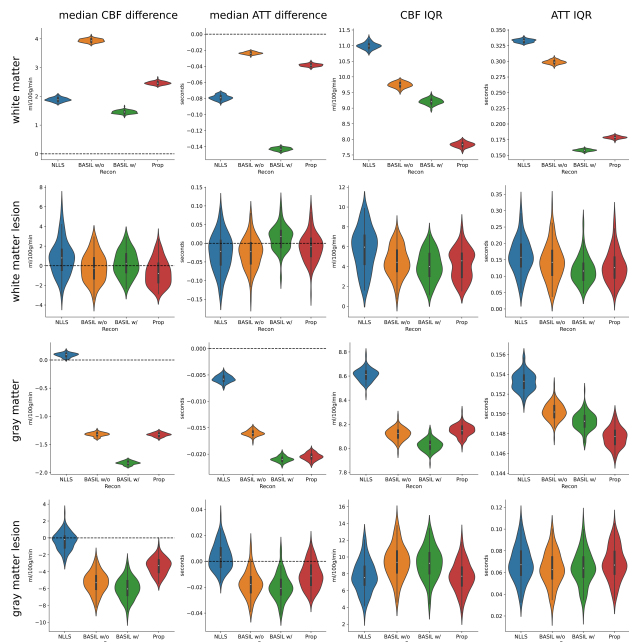


Fig. 7. Violin-plots for median differences in the median and IQR of the simulated phantom Case 3. The difference to the reference for the 100 median values for each of the evaluated ROIs is given in the left half of the figure. The dotted lines represent zero deviation to the reference median. The right half of the figure shows the 25%-75% IQR in each of the evaluated ROIs for the 100 runs. Mann-Whitney-U tests are used to assess if the differences are statistically significant. The corresponding adjusted p-values are given in table 2. The scale on the y-axis is non-uniform due to the large differences in observed values.

w/o shows slight blurring in CBF and only minor reduction of outliers in ATT. *BASIL w/* shows a similar reduction of outliers in CBF but much stronger smoothing of ATT. The proposed joint approach is able to maintain similar visual quality if just one average per PLD is used, reducing outliers in CBF and ATT without introducing blurring. Median and IQR of each subject are computed in WM and GM ROIs and visualized using a box-plot in figure 10. Due to a lack of ground truth values, the quantitative accuracy in the median is compared to NLLS with 4 averages (NLLS-4). The IQRs are compared to the proposed method. None of the methods shows a statistically significant difference in CBF medians after p-value correction (table 3). However, median ATT using one average shows a statistically significant differences to the NLLS reference for *BASIL w/* in WM. No statistically significant difference in IQR could be observed.

The run time for all algorithms was evaluated on a server with an Intel Core Xenon Gold CPU and an NVIDIA Titan XP GPU. The NLLSQ took 8 min 40 s independent of the number

of averages used. *BASIL* with one spatial prior needs 2 min 36 s using one average as input and 6 min 20 s using four averages. The run time for *BASIL* with two spatial priors was slightly higher with 2 min 41 s and 6 min 26 s for one and four averages respectively. Our algorithm took 4 min 54 s for one average and 7 min for four averages, respectively, running on a single GPU of the server at a given time. We have also evaluated the run time of our algorithm on a workstation equipped with an NVIDIA Geforce GTX 1080Ti which resulted in 4 min 20 s for 4 averages and 2 min 17s for a single average. Fitting on the GPU takes roughly 1 GB of memory. Other than sufficient memory, no hardware restrictions are present. However, the algorithm is currently only tested on NVIDIA hardware.

4.3. Stroke patients

Exemplary quantitative maps from the first patient are given in figure 11. Three slices of the central brain region clearly show reactive hyperperfusion in areas affected by the stroke or close to the stroke after successful re-canalization therapy. The corresponding arrival time is reduced, as can be seen in ATT. The area of ischemic infarction can be delineated in all fitting strategies. However, the NLLS fits are noisy and show several outliers compared to the other methods. The CBF-map estimated with *BASIL* shows no outliers but admits over-smoothing, blurring tissue boundaries compared to NLLS and the proposed method. These differences are highlighted with arrows in CBF and ATT. An exemplary slice for three additional stroke patients is given in figure 12. Differences between the methods are again highlighted by arrows. Over smoothing of CBF in both *BASIL* methods leads to a loss of small structures in the stroke area. Similar loss of detail can be observed in ATT, especially severe for *BASIL w/*. The proposed method achieves the highest contrast between GM and WM tissue without blurring or loss of structure while suppressing noise in the quantitative maps. The same behavior is observable for the remaining patients, shown in Supplementary Material Figure S6.

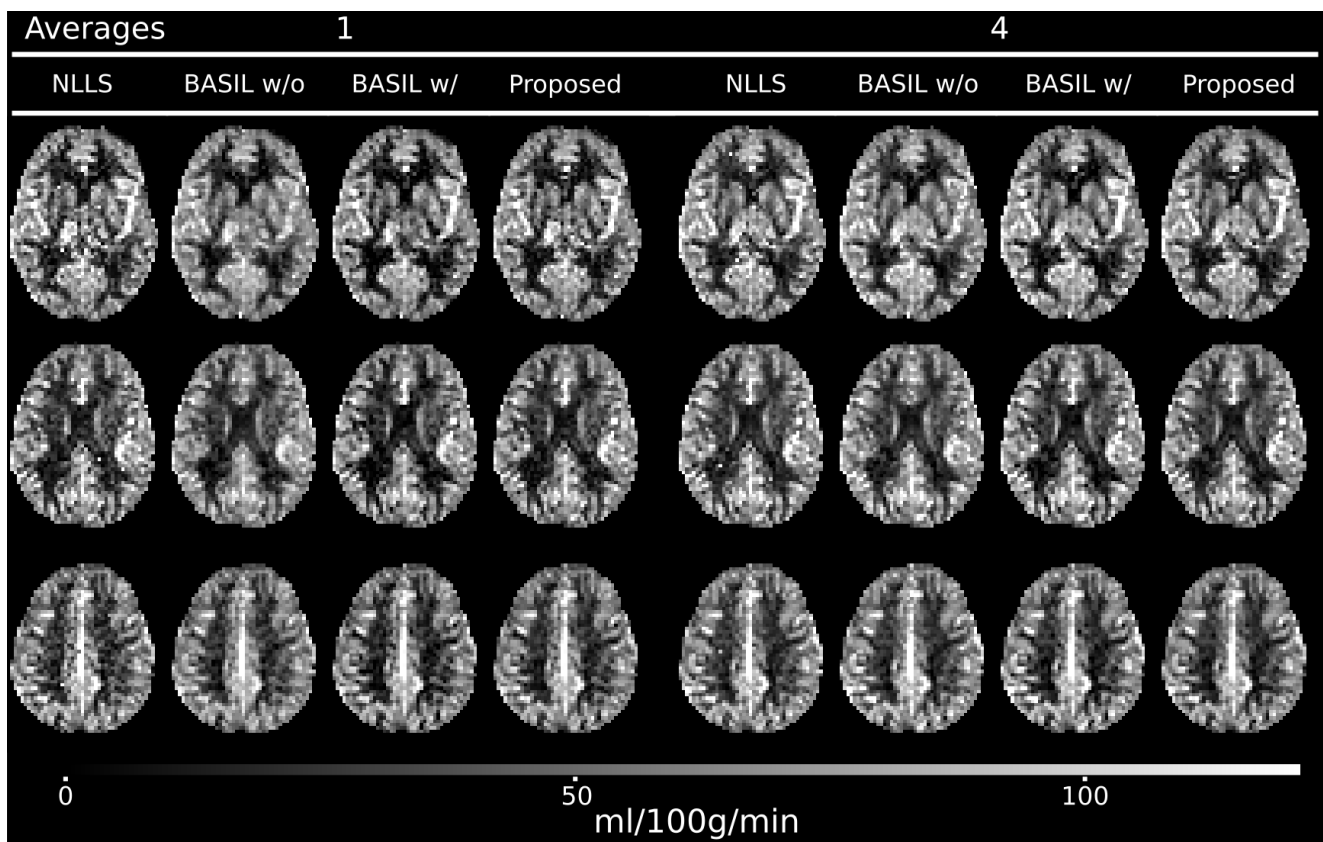


Fig. 8. Performance comparison of the four fitting algorithms in a healthy subject for a different number of averages. The CBF-maps estimated with NLLS become noisier and show more outliers as the number of averages is decreased. *BASIL w/o*, on the other hand, counteracts the worse SNR by smoothing, leading to a loss of detail in the CBF-maps. Both, *BASIL w/* and the proposed method, are able to suppress noise while maintaining high fidelity CBF-maps, independent of the number of averages.

5. Discussion

In this study we present a novel joint spatial regularization technique for quantitative ASL imaging, combining non-linear fitting with a TGV² functional. The proposed method poses a joint spatial TGV² prior on both, CBF and ATT, to improve the robustness of the fitting procedure. Synthetic ASL datasets with different pathologies as well as in vivo data from healthy and stroke patients with different SNR levels were considered.

CBF and ATT pathologies in the simulated cases could be identified in all methods. The proposed method showed an improvement in noise reduction in CBF and ATT in all simulated phantom cases. *BASIL w/* showed similar reduction of noise but leads to underestimation of high values in CBF and ATT, reflected by the increased number of points below the identity line in figure 5. This effect is less severe for *BASIL w/o* and thus might be related to the additional prior on ATT. With the exception of NLLS, all methods showed a tendency to overestimate low CBF values and underestimate high CBF values. CBF estimates of the proposed method without and with regularization on ATT produce similar results. However, joint regularization on both maps could greatly reduce noise in ATT while not showing a substantial increase in bias. This improvements of joint regularization over single regularization are in concordance with previous studies (Knoll *et al.*, 2017; Huber *et al.*, 2019; Maier *et al.*, 2018). Thus, regularization on only CBF for the proposed method is excluded in further evaluations. The joint regularization approach most accurately recovered ATT and CBF in simulated cases of partly occlusion of the arteria cerebri media, Cases 4-6 in figure 2. The visual impression is supported by the least deviations in the pixel-wise difference (figure 4) and the median and IQR values of the large stroke in table 1. Even though GM values of NLLS are closer in the median, the large IQR, especially in WM, makes interpretation of the image difficult. This effect becomes more severe for increased delays in ATT (figure 2, Case 6). Both *BASIL* approaches tend to underestimate CBF in the large stroke with increasing ATT. This might be due to the combination of spatial and non-spatial priors, assuming certain values of ATT in WM

and GM which are further smoothed by the spatial prior. As the high ATT in the simulated strokes might be well out of this range, *BASIL* is not able to recover correct ATT maps. This in turn could be the reason for the incorrect CBF estimates. The proposed approach makes no assumption of underlying CBF and ATT values and thus does not suffer as much if one parameter is strongly varied. Even though the joint regularization approach combines gradient information of both maps, no artificially introduced structures in CBF could be observed. The combined information of both structures helps in stabilizing fitting, especially in low signal areas. This joint regularization approach is advantageous compared to separate regularization (*BASIL w/*) or regularizing on one quantitative map (*BASIL w/o*, *Proposed w/o*). In Case 6 the proposed method starts to degenerate, showing an underestimation of CBF values due to the strong increase in ATT. In combination with the used LD and PLD, this strongly delayed ATT results in only few non-zero data points. Such cases require an adjustment of simulation/sequence parameters as suggested in Woods *et al.* (2018). Another simplification in our simulated phantoms affects the employed background suppression. In the simulated cases we assume instant and constant background suppression after labeling, which is not possible in practice for our used LD and PLD combinations.

As TGV² assumes piece-wise linear structures, flat areas perfectly fit this model and variations can be nearly eliminated, leading to the smallest IQRs in WM CBF and WM/GM ATTs over different noise realizations (figure 6), which is statistically significantly lower than for all other approaches (table 2). Both *BASIL* approaches are also able to reduce IQRs. The reductions are even statistically significantly lower than proposed method in the GM lesion, and in WM ATT for *BASIL w/*. For the GM lesion, *BASIL* shows a statistically significant increase in IQR over NLLS and the proposed method. Even though not visible in the median images itself, this might indicate increased blurring of CBF structures, as later seen in stroke patients in figures 11 and 12. All methods have in common that they show a statistically significant difference to the reference median in

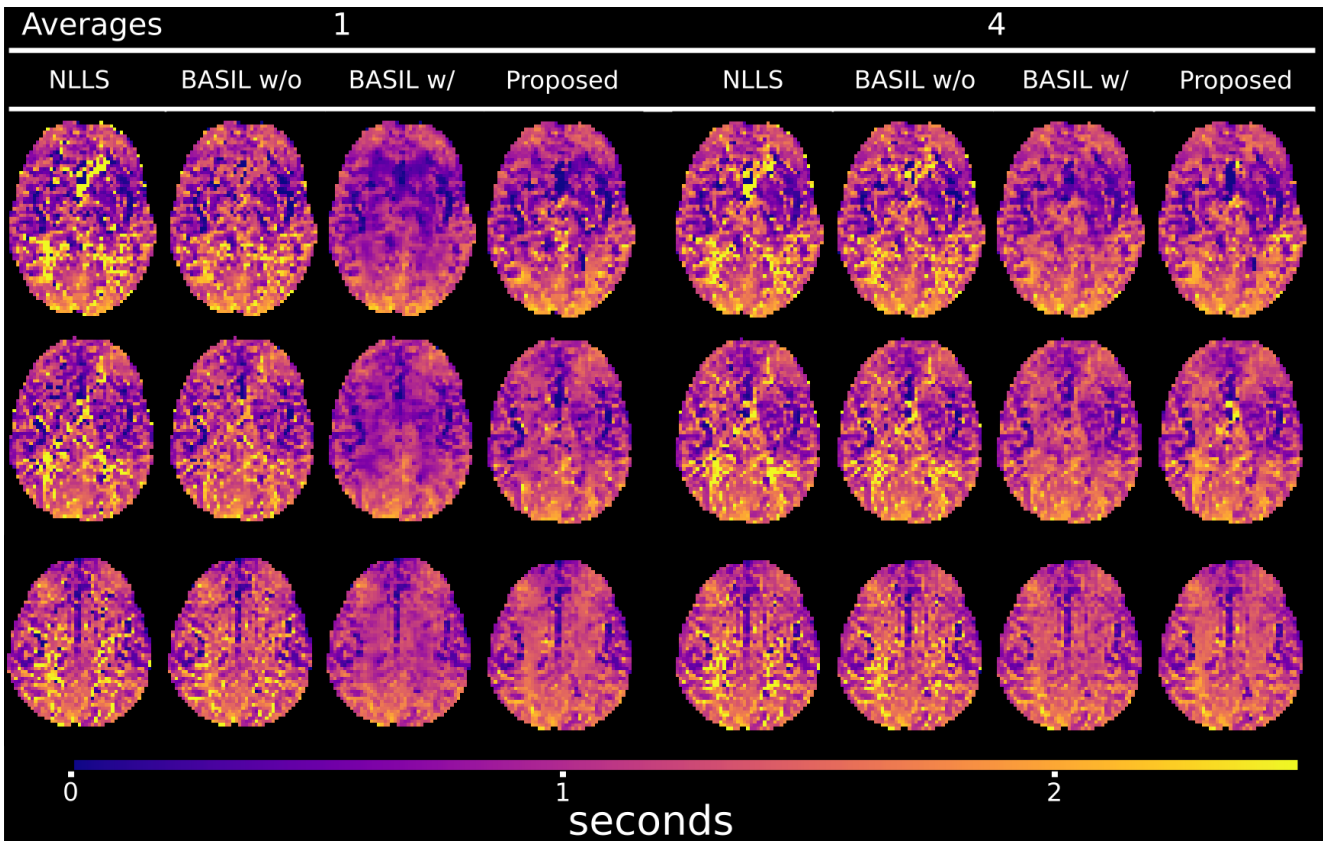


Fig. 9. ATT maps corresponding to the CBF values in figure 8. Similar to the CBF-maps, more outliers are visible in the NLLS fit if no averaging is performed. The same trends are observable for *BASIL w/o*. *BASIL w/* shows a reduction of noise in ATT but comes at the cost of slightly lower values in WM tissue. In contrast, the estimated ATT maps with the proposed method show reduced outliers and noise with only minimal loss of detail and no visually observable difference in WM values.

most cases. Deviations seem to be more severe for tissue with low SNR. As our phantom generation process mimics the MRI acquisition pipeline, noise transformation due to the multiple receive coils could be the reason for this deviations in the simulations. Such effects are more pronounced in tissue with low SNR which matches the observation of increased deviations in WM structures. Even though the proposed method takes complex noise into account, the multiple coil setting was not included. The extension to multi-coil reconstruction can be modelled by a simple multiplication of the forward model with the a priori determined receive coils and could be included in a future study.

The improved noise suppression of the proposed method in the simulated phantom may be in part due to the way the phantom has been simulated. Flat areas in CBF and ATT favour the TGV² assumptions. To mitigate this effect, phantoms were generated with fine details in high resolution (1x1x1 mm³) followed by down sampling to ASL resolution. This gives smoother transitions at tissue boundaries and reduces the amount of completely flat areas, which is reflected by the variation present in the reference itself (table 1). The influence is higher in gray matter as it consists of fewer voxels, compared to white matter.

Imposing prior knowledge on the unknown parameter maps leads to the fundamental problem of bias/variance trade-off, as the solution will depend on the used prior information. This is also true for the used MAP-based approach shown in this work. The amount of bias, however, can be controlled by the used prior and the weight between data and prior information in optimization, respectively (Brinkmann *et al.*, 2017). To this end, the NLLS approach without any regularization can be considered bias free in the mean value under the assumption of Gaussian noise. As we have seen in the phantom study, violation of this noise assumption can lead to a statistically significant bias for all methods. However, due to the lack of ground truth values for in vivo measurements and the wide spread use of NLLS we consider NLLS values for the case of four averages as our reference values for GM and WM. Using NLLS as reference is

further strengthened by the overall least deviations to identity in our 2D histogram of all simulation cases (figure 5).

CBF estimates of all methods match closely for four averages (figure 8), showing only minor noise in NLLS. Using a single average, NLLS shows increased noise while *BASIL w/o* shows slight blurring of CBF. No visual differences between *BASIL w/* and the proposed method are observable. Both show clear structures with good noise suppression. None of the methods showed a statistically significant difference to the median of NLLS in our six subjects (table 3). A slight reduction of median CBF in WM and GM of *BASIL w/* can be seen as well as an increase in WM CBF in *BASIL w/o*, which both are not statistically significant. ATT in figure 9 shows similar results. *BASIL w/* and the proposed method can reduce noise in ATT but the proposed method is simultaneously maintaining the correct median value in WM ATT. The proposed method shows no tendency to increased over- or underestimation in dependence on the number of used averages (figure 10). In contrast to the simulation study, no statistically significant reduction in IQR could be observed with the proposed method. The small number of healthy subjects (six) for this evaluation limits the statistical power as physiological variance between subjects (Henriksen *et al.*, 2012; Heijtel *et al.*, 2014) may dominate effects introduced by the different fitting methods. We expect that differences become statistically significant if the number of subjects is increased as certain trends can be seen in figure 10.

In general, the deviations of the fits are higher in WM compared to GM due to three times lower signal and additionally longer arterial transit time resulting in a lower SNR. For high SNR regimes (4 averages as well as in GM) the performance of the methods is close to each other. However, the smallest deviations are achieved with the proposed method, even though we could not show statistical significance. The advantage of posing a joint regularization becomes especially clear in low SNR areas such as WM and in the ATT maps. Leveraging all available spatial information drastically improves noise suppression and outlier elimination even if a very limited amount of data is used, as in stroke patients in figure 11 and 12. This leads to

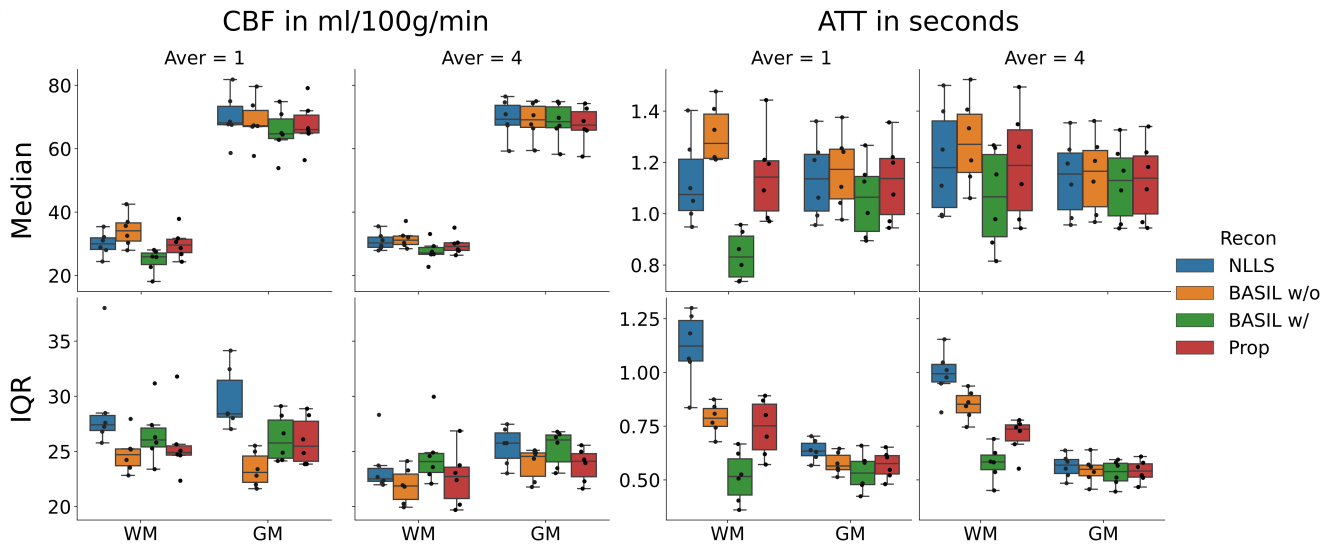


Fig. 10. Box-plot for median and IQR in white and gray matter CBF and ATT, respectively. Black dots correspond to mean or IQR of the six individual healthy subjects within the specified ROI. ROIs are defined by GM and WM mask, generated from co-registered T_1 images. Median and IQR are tested for statistically significant differences using a Mann-Whitney-U test. The corresponding p-values are given in table 3.

a clear delineation of GM and WM compared to the reference methods.

Compared to NLLS, CBF and ATT maps of the proposed method show a reduction in noise and outliers in all stroke patients (figure 11). As highlighted by arrows, the proposed method is able to recover fine details which are lost in the other regularized approaches but visible in NLLS. This loss of details may hamper detection, or even lead to a complete removal of structures in areas affected by the stroke. While all regularized approaches can reduce noise in CBF and ATT, the proposed method recover such fine structures best, as highlighted by arrows in figure 12. These differences are most severe in the patient in the third line, leading to a complete miss of certain structures close to the affected area.

The utilized CAIPIRINHA accelerated 3D single-shot acquisition is especially important for patients where subject movement can lead to uninterpretable CBF and ATT maps. Due to the single shot acquisition it is possible to account for subject motion prior to fitting. Careful selection of imaging parameters is necessary to avoid excessive blurring in slice direction. For the employed sequence, minor blurring can be seen in sagittal views (Supplementary Material Figure S7). Additionally, the employed sequence provides a more flexible approach for multi-PLD data, allowing to sample a broader range of the in-

flowing blood, which could be especially beneficial for patients where the transit time varies over a broad range. However, the improved temporal resolution using 4-fold acceleration comes at the cost of a reduced SNR which either requires a dedicated denoising step prior to fitting or makes robust parameter quantification necessary. In contrast to denoising a direct fitting approach offers the advantage of the inclusion of the signal equation which serves as additional a priori knowledge, further stabilizing the fit.

Compared to BASIL, the current method only implements the simple ASL model given in equation 2, whereas BASIL allows for simultaneous fitting of CBF, ATT, and the arterial inflow contribution in vessels. To facilitate a fair comparison this functionality of BASIL was not used in the shown fits. However, an extension to the complex model with the proposed method could be easily obtained by an adaptation of the signal equation used for fitting, which will be done in a future step. As the proposed approach has been implemented into a Python toolbox (Maier *et al.*, 2020), addition of new models can be achieved in a straight forward manner. Extension to other ASL models, e.g. pulsed ASL (PASL), is simply done by replacing the forward model in equation 2 with the appropriate one. Simple models, not consisting of composed functions, can be included using a plain text file. Complex models need to be im-

plemented in Python by the user but templates exist to help in the implementation process. A detailed description of the employed software and how to include new models can be found in Maier *et al.* (2020). An exemplary PASL fit for phantom Case 0 is given in Supplementary Material Figure S8.

In this study we employed an advanced ASL method with a flexible number of combinations of averages and PLDs. Sixteen equally spaced PLDs were used, as the range of the arterial transit time was not known in advance. Additionally, a different range of ATT is expected for healthy subjects and ischemic stroke patients where mostly a prolonged ATT is observed. Further improvements in ATT and CBF maps for all methods could be expected by optimizing the imaging protocol for the healthy and patient cohort separately using the general framework proposed by Woods *et al.* (2018).

Joint regularization could potentially lead to a feature creep from one map into another. While theoretically possible, previous work using joint regularization strategies based on the Frobenius norm have shown that such adverse effects are virtually never observed in practice (Knoll *et al.*, 2017; Huber *et al.*, 2019; Maier *et al.*, 2018). Feature creep usually occurs if reconstruction relies heavily on regularization or if the chosen regularization weight is too high for the given data and stronger coupling norms, like the Nuclear norm, are used. To investigate if feature creep occurs, we introduced Case 2 in our phantom series. The pathology in the frontal left area is clearly visible in the fitted CBF but no adverse effect can be observed in the corresponding area of ATT, neither in the quantitative map itself (figure 1) nor in the pixel wise difference (figure 3). In addition, Cases 4-6 in figure 2 and figure 4 also show no adverse effect of the imposed ATT pathology on the CBF map. The contrary can be observed, the joint regularization produces the most stable CBF estimates of all methods. A totally wrong choice of the regularization weight compared to the supporting data could nevertheless introduce such errors. However, such a strong weight for regularization would also lead to a severely hampered visual impression and such fits would likely be discarded.

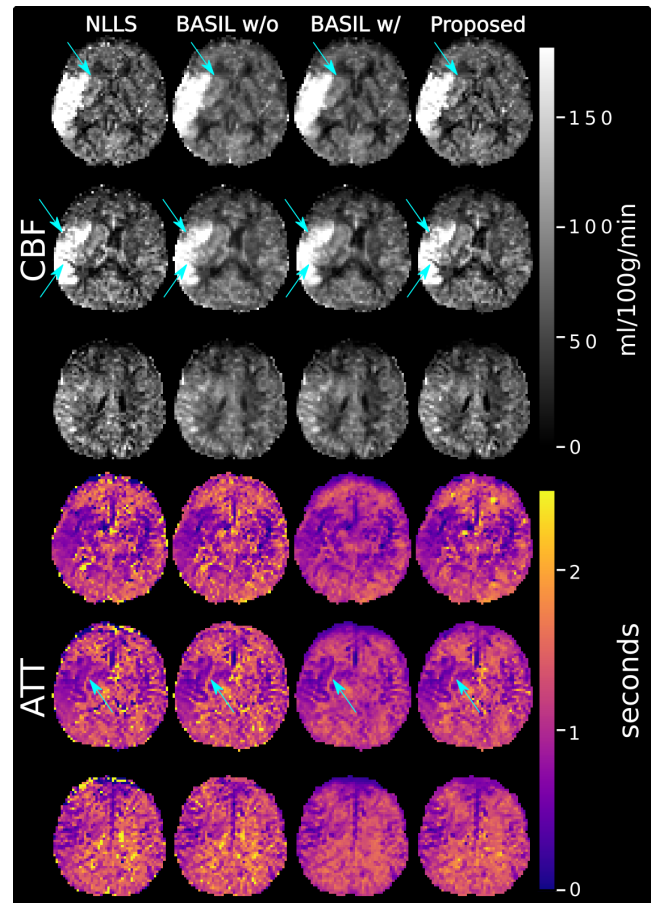


Fig. 11. CBF and ATT maps of a patient 24 hours post ischemic stroke. The reactive hyperperfusion areas after successful recanalization are clearly visible in all fits. BASIL CBF maps appear to be oversmoothed compared to NLLS and the proposed method. Especially deep brain regions show worse contrast compared to the proposed regularization strategy.

The assumption of AWGN is typically valid in the real and imaginary channel of single channel complex MRI data but violated for commonly used magnitude images, especially if array coils are used (Aja-Fernández and Tristán-Vega, 2015). Even though the AWGN assumption might be violated in the PWI series, convergence of the algorithm itself is not hampered. However, results obtained from data that violates the AWGN assumption might show some bias compared to the true value. Such bias could be avoided by adapting the data norm to account for the altered noise distribution, e.g. L^1 data norm for salt-and-pepper noise. In general, the resulting data measure need not be convex and optimization could get stuck in critical points, e.g. local minima or points of inflection, resulting in even worse fitting than the generic L^2 data norm. In addition, the L^2 -norm possesses several desirable properties for optimization (differentiability, convexity) which usually outweigh the drawback of a slight bias and is thus widely used, also in our reference methods. Nevertheless it should be noted that the optimal case for fitting complex MRI data to a given signal model would be to use the raw complex k-space signal from each receive coil separately.

A natural extension of the proposed fitting approach would be to incorporate the whole MRI signal acquisition pipeline, i.e. coil sensitivity profiles and Fourier sampling, directly fitting k-space data. This would leverage the natural Gaussian distribution present in the raw k-space signal, fully validating the choice of the L^2 -norm for fitting. Contrary to recent works on improved ASL-perfusion image reconstruction such as MOCHA (Mehranian *et al.*, 2020) or ASL-TGV (Spann *et al.*, 2020), which reconstructs the perfusion weighted images from raw k-space data, no subsequent fitting step would be required to estimate CBF and ATT. Further, noise characteristics in such improved PWI images might severely deviate from the assumption of AWGN due to the non-linear reconstruction process and might lead to a bias in the estimation process. The model based fitting approach potentially allows for higher acceleration compared to the two separate steps, image reconstruction followed by fitting, due to the reduction of un-

knowns and combination of information of the different PWIs by means of the signal equation. Further extensions of the proposed method could include partial volume correction based on two compartment models, which are already included in BASIL.

ASL imaging is very sensitive to signal variations from motion or changes in blood velocity due to the cardiac cycle (Verbee and van Osch, 2017). Currently, the proposed method does not directly account for these variations. Motion related variations are corrected for in a preprocessing step but no correction for blood velocity changes is applied. As it is planned to extend the method to use raw k-space data, motion could be included in the forward model, e.g. based on determined motion fields prior to fitting, as it is done in MOCHA. As estimation of motion directly from highly undersampled k-space data can be challenging, a robust estimation and correction needs to be found. Another possibility would be to include a motion term into the fitting process but this poses a mathematically challenging problem, especially for forming forward and adjoint operation pairs.

If ASL data is evaluated over large ROIs, NLLS seems to be the favourable method as it shows the least bias in our simulations (figure 7) for most investigated ROIs, especially in GM. However, this might only be advantageous if a large population of subjects is used. Single reconstruction can be subject of significant noise, as reflected by the highest IQR of all methods. The proposed approach is preferable in single observation scenarios as it shows comparable bias to the other methods but generally the least deviations (IQR). Even though *BASIL w/* can reduce IQR to a similar range as the proposed method, it shows the highest bias of all investigated algorithms in most cases, especially in ATT.

In addition to the 3D acquisition used in this work, ASL is often performed in a 2D slice-by-slice fashion. Such data can also be fitted with the presented reconstruction framework, either, by applying regularization in 2D only or by adapting the third gradient direction to account for non-isotropic voxels. This adaptation amounts to a simple scaling of the gradient with respect

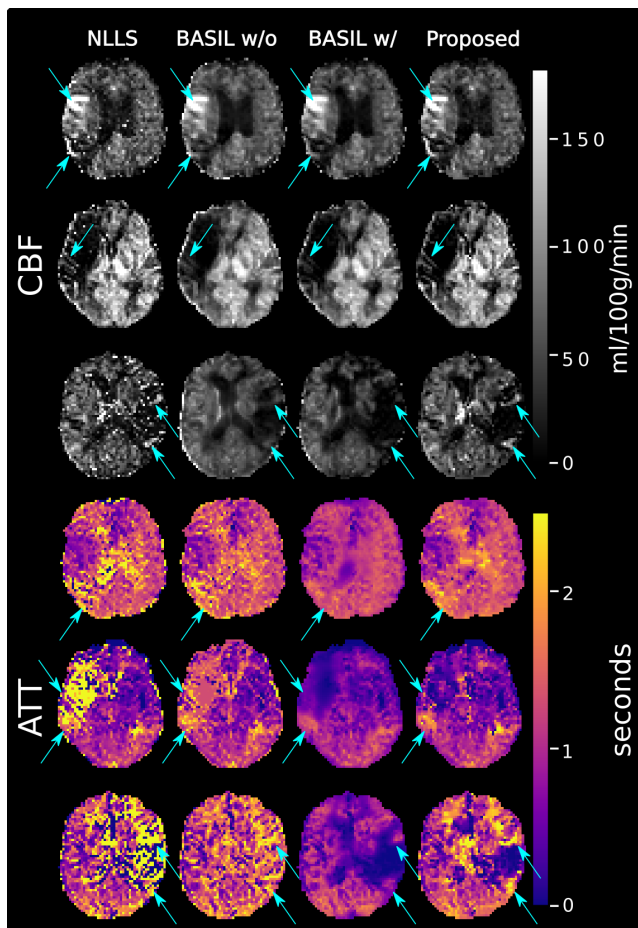


Fig. 12. An exemplary slice of CBF and ATT for three selected stroke patients. Patients are shown in rows, different reconstruction methods in columns. Difference between methods are highlighted by arrows.

to the ratio between in-plane and the acquired slice resolution, taking into account slice thickness and inter slice gap. Setting this scaling to zero equals 2D regularization. However, 3D regularization outperforms 2D, as has been shown in previous work (Huber *et al.*, 2019; Maier *et al.*, 2018).

Reconstruction on the GPU required roughly 1 GB of memory which should be available on any recent GPU. Computation speed varies with hardware and further reduction could be expected with the recent increase in GPU performance. If memory requirements supersede the available GPU memory, a double buffering strategy is available, as introduced in Maier *et al.* (2020). New scanner consoles already often include GPUs, thus the proposed method could be directly integrated into the scanner reconstruction process.

6. Conclusion

The proposed non-linear fitting approach with joint spatial priors on CBF and ATT provides high-quality quantitative maps of the whole brain from a single-shot 3D acquisition. The combination of single-shot 3D acquisition and robust parameter quantification addresses important clinical demands in terms of motion robustness, scan-time reduction and a much better sampling of the kinetic curve. This makes this approach promising for challenging image acquisition conditions of patients with cerebrovascular disease.

Acknowledgments

The authors would like to acknowledge Dr. Marta Vidorreta Diaz De Cerio, Siemens Healthcare, Spain for providing the updated pCASL module with improved background suppression.

We would like to thank Lukas Pirpamer from the Medical University Graz for assistance in data export.

Funding

Oliver Maier is a recipient of a DOC Fellowship (24966) of the Austrian Academy of Sciences at the Institute of Medical Engineering at TU Graz. The authors would like to acknowledge the NVIDIA Corporation Hardware grant support.

Appendix A. Mathematical derivations

As described in section 2.5 it is our goal to solve the following optimization task within each GN iteration

$$\begin{aligned} \min_{u,v} \quad & \frac{1}{2} \sum_{n=1}^{N_d} \|DA_{\phi,t_n}|_{u=u^k} u - \tilde{d}_n^k\|_2^2 + \\ & \gamma_k(\beta_0 \|\nabla u - v\|_{1,2,F} + \beta_1 \|\mathcal{E}v\|_{1,2,F}) + \\ & \frac{\delta_k}{2} \|u - u^k\|_{M_k}^2, \end{aligned} \quad (\text{A.1})$$

where $\nabla : U^{N_u} \rightarrow U^{3 \times N_u}$ and $\mathcal{E} : U^{3 \times N_u} \rightarrow U^{6 \times N_u}$ are defined as

$$\nabla u = (\delta_{i+} u^l, \delta_{j+} u^l, \delta_{k+} u^l)_{l=1}^{N_u}$$

and

$$\mathcal{E}v = \left(\delta_{i-} v^{1,l}, \delta_{j-} v^{2,l}, \delta_{k-} v^{3,l}, \right. \\ \left. \frac{\delta_{j-} v^{1,l} + \delta_{i-} v^{2,l}}{2}, \frac{\delta_{k-} v^{1,l} + \delta_{i-} v^{3,l}}{2}, \frac{\delta_{k-} v^{2,l} + \delta_{j-} v^{3,l}}{2} \right)_{l=1}^{N_u}.$$

The operators δ_{i+} , δ_{j+} , δ_{k+} and δ_{i-} , δ_{j-} , δ_{k-} define forward and backward finite difference operators, respectively, with respect to the i , j and k coordinate. The image is symmetrically extended outside the domain.

The required saddle point formulation of the form,

$$\min_x \max_y \langle Kx, y \rangle + G(x) - F^*(y), \quad (\text{A.2})$$

equivalent to Eq. 8 can be obtained using the convex conjugate as follows:

$$\begin{aligned} \min_{x=(u,v)} \quad & \frac{1}{2} \sum_{n=1}^{N_d} \|DA_{\phi,t_n}|_{u=u^k} u - \tilde{d}_n^k\|_2^2 + \\ & \gamma_k(\beta_0 \|\nabla u - v\|_{1,2,F} + \beta_1 \|\mathcal{E}v\|_{1,2,F}) + \\ & \frac{\delta_k}{2} \|u - u^k\|_{M_k}^2 \\ \Leftrightarrow \min_x \max_{y=(z_0,z_1,r)} \quad & \sum_{n=1}^{N_d} \left\{ \langle DA_{\phi,t_n}|_{u=u^k} u, r_n \rangle - \langle \tilde{d}_n^k, r_n \rangle - \frac{1}{2} \|r_n\|_2^2 \right\} + \\ & \langle K_1 x, z \rangle - \mathcal{I}_{\{\|\cdot\|_{\infty} \leq \beta_0 \gamma_k\}}(z_0) - \mathcal{I}_{\{\|\cdot\|_{\infty} \leq \beta_1 \gamma_k\}}(z_1) \\ & + \frac{\delta_k}{2} \|u - u^k\|_{M_k}^2 \\ \Leftrightarrow \min_x \max_y \quad & \langle Kx, y \rangle + G(x) - F^*(y). \end{aligned}$$

with

$$K = \begin{pmatrix} DA_{\phi} & 0 \\ \nabla & -id \\ 0 & \mathcal{E} \end{pmatrix}, \quad K_1 = \begin{pmatrix} \nabla & -id \\ 0 & \mathcal{E} \end{pmatrix}, \quad z = (z_0, z_1).$$

id amounts to the identity matrix. $F^*(y) = F^*(z_0, z_1, r) = \sum_{n=1}^{N_d} \left\{ \langle \tilde{d}_n^k, r_n \rangle + \frac{1}{2} \|r_n\|_2^2 \right\} + \mathcal{I}_{\{\|\cdot\|_{\infty} \leq \beta_0 \gamma_k\}}(z_0) + \mathcal{I}_{\{\|\cdot\|_{\infty} \leq \beta_1 \gamma_k\}}(z_1)$, and $G(x) = G(u) = \frac{\delta_k}{2} \|u - u^k\|_{M_k}^2$. $\mathcal{I}_{\{\|\cdot\|_{\infty} \leq \beta_p \gamma_k\}}(z_p)$ amounts to the convex conjugate of the L^1 -norm which is defined as the indicator function of the unit ball of the L^∞ -norm scaled with the corresponding regularization parameter $\beta_p \gamma$ ($p = 0, 1$)

$$\mathcal{I}_{\{\|\cdot\|_{\infty} \leq \beta_p \gamma_k\}}(z_p) = \begin{cases} 0 & \|z_p\|_{\infty} \leq \beta_p \gamma_k \\ \infty & \text{else} \end{cases}$$

$DA_{\phi,t_n}|_{u=u^k}$ is the Jacobian matrix evaluated at $u = u^k$ of the non-linear ASL signal equation for all scans n_t :

$$DA_{\phi} : u = (u_l)_{l=1}^{N_u} \mapsto \left(\sum_{l=1}^{N_u} \left[\frac{\partial A_{\phi,t_n}(u)}{\partial u_l} \Big|_{u=u^k} u_l \right] \right)_{n=1}^{N_d} = (\eta_n)_{n=1}^{N_d}. \quad (\text{A.3})$$

To compute the update steps of the PD algorithm as

$$\begin{aligned} y^{n+1} &= (id + \sigma \partial F^*)^{-1} (y^n + \sigma K \bar{x}^n) \\ x^{n+1} &= (id + \tau \partial G)^{-1} (x^n - \tau K^H y^{n+1}) \\ \bar{x}^{n+1} &= x^{n+1} + \theta (x^{n+1} - x^n) \end{aligned} \quad (\text{A.4})$$

with $\theta \in [0, 1]$, the following operations need to be defined.

The adjoint operations of K , K^H are

$$K^H = \begin{pmatrix} DA_{\phi}^H & -\text{div}^1 & 0 \\ 0 & -id & -\text{div}^2 \end{pmatrix}, \quad (\text{A.5})$$

where the divergence operators div^1 and div^2 are the negative adjoints of ∇ and \mathcal{E} , respectively. The adjoint of DA_{ϕ} reads as

$$DA_{\phi}^H : \eta = (\eta_n)_{n=1}^{N_d} \mapsto \left(\sum_{n=1}^{N_d} \frac{\partial A_{\phi,t_n}(u)}{\partial u_l} \Big|_{u=u^k} \eta_n \right)_{l=1}^{N_u} = (u_l)_{l=1}^{N_u} = u.$$

The operators P corresponding to the proximal mapping of F^* , i.e. the convex conjugate of F , and G in the algorithm are given by

$$(id + \sigma \partial F^*)^{-1}(\xi) := \begin{cases} P_{\beta_0}(\xi_0) = \frac{\xi_0}{\max\left(1, \frac{|\xi_0|}{\beta_0 \gamma_k}\right)} \\ P_{\beta_1}(\xi_1) = \frac{\xi_1}{\max\left(1, \frac{|\xi_1|}{\beta_1 \gamma_k}\right)} \\ P_{\sigma L^2}(\xi_2) = \frac{\xi_2 - \sigma d^k}{1 + \sigma} \end{cases}$$

$$(id + \tau \partial G)^{-1}(\xi) := P_{\tau G}(\xi) = (id + \tau \delta_k M_k)^{-1}(\tau \delta_k M_k u^k + \xi)$$

where the operations in $P_{\beta_0}(\xi_1)$, $P_{\beta_1}(\xi_2)$, and $P_{\sigma L^2}(\xi_3)$ are performed point wise. The multiplication with M_k can be easily computed as M_k is a diagonal matrix. The inversion of $(id + \tau \delta_k M_k)$ is simply a inversion of each element on the diagonal. Thus $P_{\tau G}(\xi)$ can be computed easily in a point-wise fashion.

Appendix B. Pseudo Code

```

1 Initialize:  $(u^0, v^0), (\bar{u}^0, \bar{v}^0), (z_0^0, z_1^0, r^0), \tau^0 > 0,$ 
    $\kappa = 1, \theta^0 = 1, \mu = 0.5, \delta = 0.99$ 
2 for  $m \leftarrow 0$  to  $maxit$  do
3   Primal Update:
4      $u^{m+1} \leftarrow P_{\tau^m G} \left( u^m - \tau^m \left( -\text{div}^1 z_0^m + \text{DA}_\phi^H r^m \right) \right)$ 
5      $v^{m+1} \leftarrow v - \tau^m \left( -\text{div}^2 z_1^m - z_0^m \right)$ 
6   Update  $\tau$ :
7      $\tau^{m+1} \leftarrow \tau^m \sqrt{1 + \theta^m}$ 
8   Start Linesearch:
9     Update  $\theta$ :
10     $\theta^{m+1} \leftarrow \frac{\tau^{m+1}}{\tau^m}$ 
11   Extrapolation:
12     $(\bar{u}^{m+1}, \bar{v}^{m+1}) \leftarrow$ 
    $(u^{m+1}, v^{m+1}) + \theta^{m+1}((u^{m+1}, v^{m+1}) - (u^m, v^m))$ 
13   Dual Update:
14     $z_0^{m+1} \leftarrow P_{\beta_0} \left( z_0^m + \kappa \tau^{m+1} (\nabla \bar{u}^{m+1} - \bar{v}^{m+1}) \right)$ 
15     $z_1^{m+1} \leftarrow P_{\beta_1} \left( z_1^m + \kappa \tau^{m+1} (\mathcal{E} \bar{v}^{m+1}) \right)$ 
16     $r^{m+1} \leftarrow P_{\kappa \tau^{m+1} L^2} \left( r^m + \kappa \tau^{m+1} (\text{DA}_\phi \bar{u}^{m+1}) \right)$ 
17   break Linesearch if:
18     $\sqrt{\kappa} \tau^{m+1} \|K^H y^{m+1} - K^H y^m\|_2 \leq \delta \|y^{m+1} - y^m\|_2$ 
19   else:
20     $\tau^{m+1} \leftarrow \tau^{m+1} \mu$ 

```

Algorithm 1: Primal-dual algorithm for solving the TGV² regularized ASL parameter quantification task in every Gauss-Newton step. Note that linearity of involved operations can be used to decrease computational load.

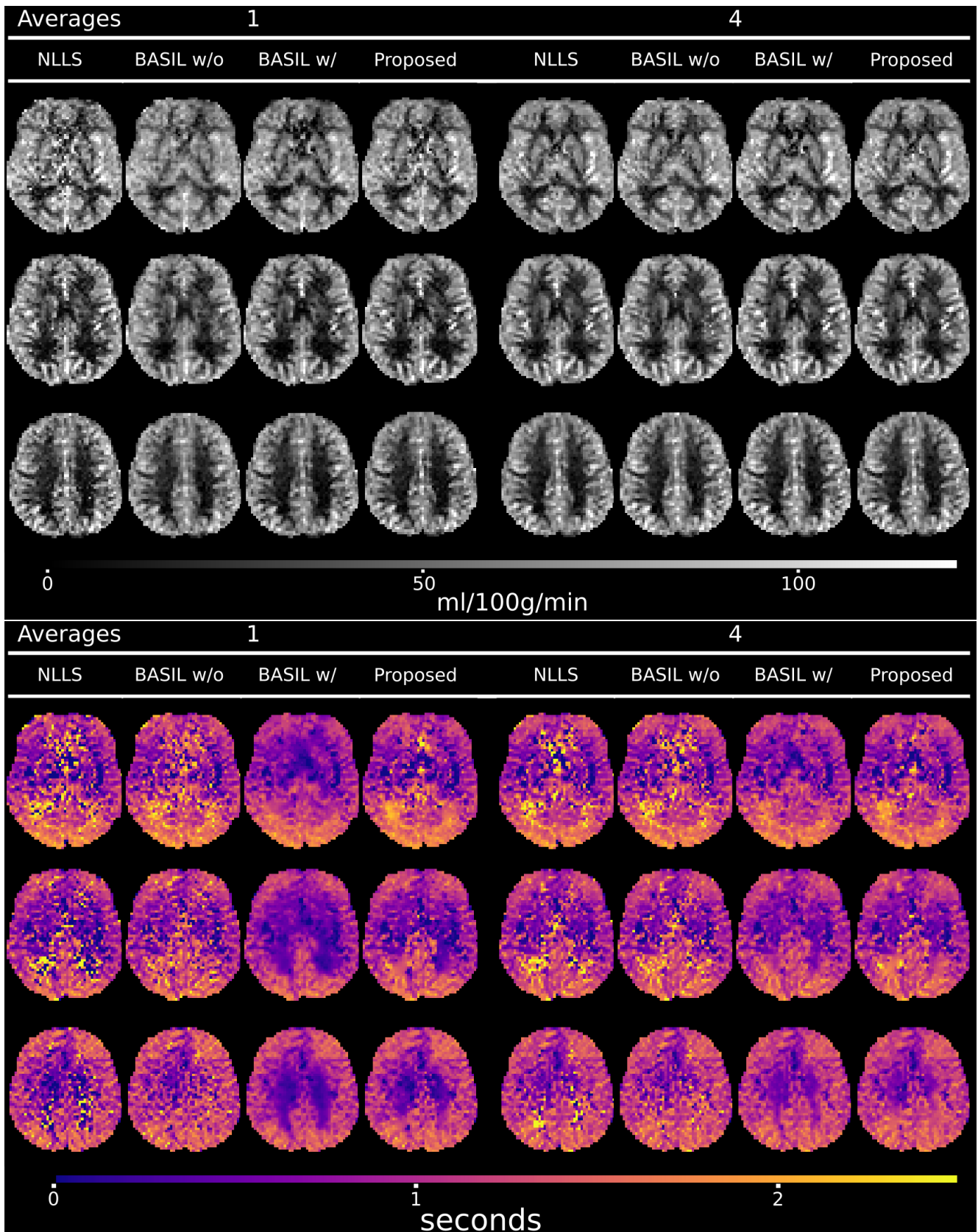
References

- Aja-Fernández, S., Tristán-Vega, A., 2015. A review on statistical noise models for Magnetic Resonance Imaging. LPI, ETSI Telecomunicación, Univ. Valladolid, Spain, Tech. Rep.
- Alsop, D.C., Detre, J.A., Golay, X., Günther, M., Hendrikse, J., Hernandez-Garcia, L., Lu, H., MacIntosh, B.J., Parkes, L.M., Smits, M., van Osch, M.J.P., Wang, D.J.J., Wong, E.C., Zaharchuk, G., 2014. Recommended implementation of arterial spin-labeled perfusion MRI for clinical applications: A consensus of the ISMRM perfusion study group and the european consortium for ASL in dementia. *Magnetic Resonance in Medicine* 73, 102–116. URL: <https://doi.org/10.1002/mrm.25197>, doi:10.1002/mrm.25197.
- Bakushinsky, A.B., Kokurin, M.Y., 2004. Iterative Methods for Approximate Solution of Inverse Problems. Springer Netherlands. URL: <https://doi.org/10.1007/978-1-4020-3122-9>, doi:10.1007/978-1-4020-3122-9.
- Boland, M., Stirnberg, R., Pracht, E.D., Kramme, J., Viviani, R., Stingl, J., Stöcker, T., 2018. Accelerated 3d-GRASE imaging improves quantitative multiple post labeling delay arterial spin labeling. *Magnetic Resonance in Medicine* 80, 2475–2484. URL: <https://doi.org/10.1002/mrm.27226>, doi:10.1002/mrm.27226.
- Bonferroni, C.E., 1936. Teoria statistica delle classi e calcolo delle probabilità. volume 8. Libreria internazionale Seeber.
- Bredies, K., 2014. Recovering piecewise smooth multichannel images by minimization of convex functionals with total generalized variation penalty, in: Efficient Algorithms for Global Optimization Methods in Computer Vision. Springer Berlin Heidelberg, pp. 44–77. URL: https://doi.org/10.1007/978-3-642-54774-4_3, doi:10.1007/978-3-642-54774-4_3.
- Bredies, K., Kunisch, K., Pock, T., 2010. Total generalized variation. *SIAM Journal on Imaging Sciences* 3, 492–526. URL: <https://doi.org/10.1137/090769521>, doi:10.1137/090769521.
- Brinkmann, E.M., Burger, M., Rasch, J., Sutour, C., 2017. Bias reduction in variational regularization. *Journal of Mathematical Imaging and Vision* 59, 534–566. URL: <https://doi.org/10.1007/s10851-017-0747-z>, doi:10.1007/s10851-017-0747-z.
- Buxton, R.B., Frank, L.R., Wong, E.C., Siewert, B., Warach, S., Edelman, R.R., 1998. A general kinetic model for quantitative perfusion imaging with arterial spin labeling. *Magnetic Resonance in Medicine* 40, 383–396. URL: <https://doi.org/10.1002/mrm.1910400308>, doi:10.1002/mrm.1910400308.
- Chambolle, A., Pock, T., 2010. A first-order primal-dual algorithm for convex problems with applications to imaging. *Journal of Mathematical Imaging and Vision* 40, 120–145. URL: <https://doi.org/10.1007/s10851-010-0251-1>, doi:10.1007/s10851-010-0251-1.
- Chappell, M., Groves, A., Whitcher, B., Woolrich, M., 2009. Variational bayesian inference for a nonlinear forward model. *IEEE Transactions on Signal Processing* 57, 223–236. URL: <https://doi.org/10.1109/tsp.2008.2005752>, doi:10.1109/tsp.2008.2005752.
- Chappell, M.A., Groves, A.R., MacIntosh, B.J., Donahue, M.J., Jezzard, P., Woolrich, M.W., 2011. Partial volume correction of multiple inversion time arterial spin labeling MRI data. *Magnetic Resonance in Medicine* 65, 1173–1183. URL: <https://doi.org/10.1002/mrm.22641>, doi:10.1002/mrm.22641.
- Chappell, M.A., MacIntosh, B.J., Donahue, M.J., Günther, M., Jezzard, P., Woolrich, M.W., 2010. Separation of macrovascular signal in multi-inversion time arterial spin labelling MRI. *Magnetic Resonance in Medicine* 63, 1357–1365. URL: <https://doi.org/10.1002/mrm.22320>, doi:10.1002/mrm.22320.
- Dai, W., Garcia, D., de Bazelaire, C., Alsop, D.C., 2008. Continuous flow-driven inversion for arterial spin labeling using pulsed radio frequency and gradient fields. *Magnetic Resonance in Medicine* 60, 1488–1497. URL: <https://doi.org/10.1002/mrm.21790>, doi:10.1002/mrm.21790.
- Dai, W., Robson, P.M., Shankaranarayanan, A., Alsop, D.C., 2011. Reduced resolution transit delay prescan for quantitative continuous arterial spin labeling perfusion imaging. *Magnetic Resonance in Medicine* 67, 1252–1265. URL: <https://doi.org/10.1002/mrm.23103>, doi:10.1002/mrm.23103.
- Deledalle, C.A., Papadakis, N., Salmon, J., Vaiter, S., 2017. CLEAR: Covariant LEAsT-square refitting with applications to image restoration. *SIAM Journal on Imaging Sciences* 10, 243–284. URL: <https://doi.org/10.1137/16m1080318>, doi:10.1137/16m1080318.
- Detre, J.A., Leigh, J.S., Williams, D.S., Koretsky, A.P., 1992. Perfusion imaging. *Magnetic Resonance in Medicine* 23, 37–45. URL: <https://doi.org/10.1002/mrm.1910230106>, doi:10.1002/mrm.1910230106.
- Donoho, D., 2006. Compressed sensing. *IEEE Transactions on Information Theory* 52, 1289–1306. URL: <https://doi.org/10.1109/tit.2006.871582>, doi:10.1109/tit.2006.871582.
- Feinberg, D., Ramann, S., Gunther, M., 2009. Evaluation of new ASL 3D GRASE sequences using Parallel Imaging, Segmented and Interleaved k-space at 3T with 12- and 32-channel Coils. *Proc. Intl. Soc. Mag. Reson. Med.* 17.
- Friston, K., Ashburner, J., Kiebel, S., Nichols, T., Penny, W. (Eds.), 2007. Statistical Parametric Mapping. Elsevier. URL: <https://linkinghub.elsevier.com/retrieve/pii/B9780123725608X50001>, doi:10.1016/B978-0-12-372560-8.X5000-1.
- Greve, D.N., Fischl, B., 2009. Accurate and robust brain image alignment using boundary-based registration. *NeuroImage* 48, 63–72. URL: <https://doi.org/10.1016/j.neuroimage.2009.06.060>, doi:10.1016/j.neuroimage.2009.06.060.
- Groves, A.R., Chappell, M.A., Woolrich, M.W., 2009. Combined spatial and non-spatial prior for inference on MRI time-series. *NeuroImage* 45, 795–809. URL: <https://doi.org/10.1016/j.neuroimage.2008.12.027>, doi:10.1016/j.neuroimage.2008.12.027.
- Günther, M., Oshio, K., Feinberg, D.A., 2005. Single-shot 3d imaging techniques improve arterial spin labeling perfusion measurements. *Magnetic Resonance in Medicine* 54, 491–498. URL: <https://doi.org/10.1002/mrm.20580>, doi:10.1002/mrm.20580.
- Heijtel, D., Mutsaerts, H., Bakker, E., Schober, P., Stevens, M., Petersen, E., van Berckel, B., Majoie, C., Booi, J., van Osch, M., van Bavel, E., Boellaard, R., Lammertsma, A., Nederveen, A., 2014. Accuracy and precision of pseudo-continuous arterial spin labeling perfusion during baseline and hypercapnia: A head-to-head comparison with 15o h2o positron emission tomography. *NeuroImage* 92, 182–192. URL: <https://doi.org/10.1016/j.neuroimage.2014.02.011>, doi:10.1016/j.neuroimage.2014.02.011.
- Henriksen, O.M., Larsson, H.B., Hansen, A.E., Grüner, J.M., Law, I., Rosstrup, E., 2012. Estimation of intersubject variability of cerebral blood flow measurements using MRI and positron emission tomography. *Journal of Magnetic Resonance Imaging* 35, 1290–1299. URL: <https://doi.org/10.1002/jmri.23579>, doi:10.1002/jmri.23579.
- Herscovitch, P., Raichle, M.E., 1985. What is the correct value for the brain-blood partition coefficient for water? *Journal of Cerebral Blood Flow & Metabolism* 5, 65–69. URL: <https://doi.org/10.1038/jcbfm.1985.9>, doi:10.1038/jcbfm.1985.9.
- Huber, R., Haberfehlner, G., Holler, M., Kothleitner, G., Bredies, K., 2019. Total generalized variation regularization for multi-modal electron tomography. *Nanoscale* 11, 5617–5632. URL: <https://doi.org/10.1039/c8nr09058k>, doi:10.1039/c8nr09058k.
- Ivanov, D., Pfeuffer, J., Gardumi, A., Uludağ, K., Poser, B.A., 2017. 2D CAIPIRINHA improves accelerated 3D GRASE ASL, in: Proc. 25th Annu. Meet. ISMRM, Honolulu, 2017, p. 3630. URL: <http://indexsmart.miramir.com/ISMRM2017/PDFfiles/3630.html>.
- Jenkinson, M., Bannister, P., Brady, M., Smith, S., 2002. Improved optimization for the robust and accurate linear registration and motion correction of brain images. *NeuroImage* 17, 825–841. URL: <https://doi.org/10.1006/nimg.2002.1132>, doi:10.1006/nimg.2002.1132.
- Jenkinson, M., Beckmann, C.F., Behrens, T.E., Woolrich, M.W., Smith, S.M., 2012. FSL. *NeuroImage* 62, 782–790. URL: <https://doi.org/10.1016/j.neuroimage.2011.09.015>, doi:10.1016/j.neuroimage.2011.09.015.
- Jenkinson, M., Smith, S., 2001. A global optimisation method for robust affine registration of brain images. *Medical Image Analysis* 5, 143–156. URL: [https://doi.org/10.1016/s1361-8415\(01\)00036-6](https://doi.org/10.1016/s1361-8415(01)00036-6), doi:10.1016/s1361-8415(01)00036-6.
- Kaltenbacher, B., Hofmann, B., 2010. Convergence rates for the iteratively regularized gauss-newton method in banach spaces. *Inverse Problems* 26, 035007. URL: <https://doi.org/10.1088/0266-5611/26/3/035007>, doi:10.1088/0266-5611/26/3/035007.
- Kaltenbacher, B., Neubauer, A., Scherzer, O., 2008. Iterative Regularization Methods for Nonlinear Ill-Posed Problems. De Gruyter, Berlin, Boston. URL: <https://doi.org/10.1515/9783110208276>, doi:10.1515/9783110208276.
- Klößner, A., Pinto, N., Lee, Y., Catanzaro, B., Ivanov, P., Fasih, A.,

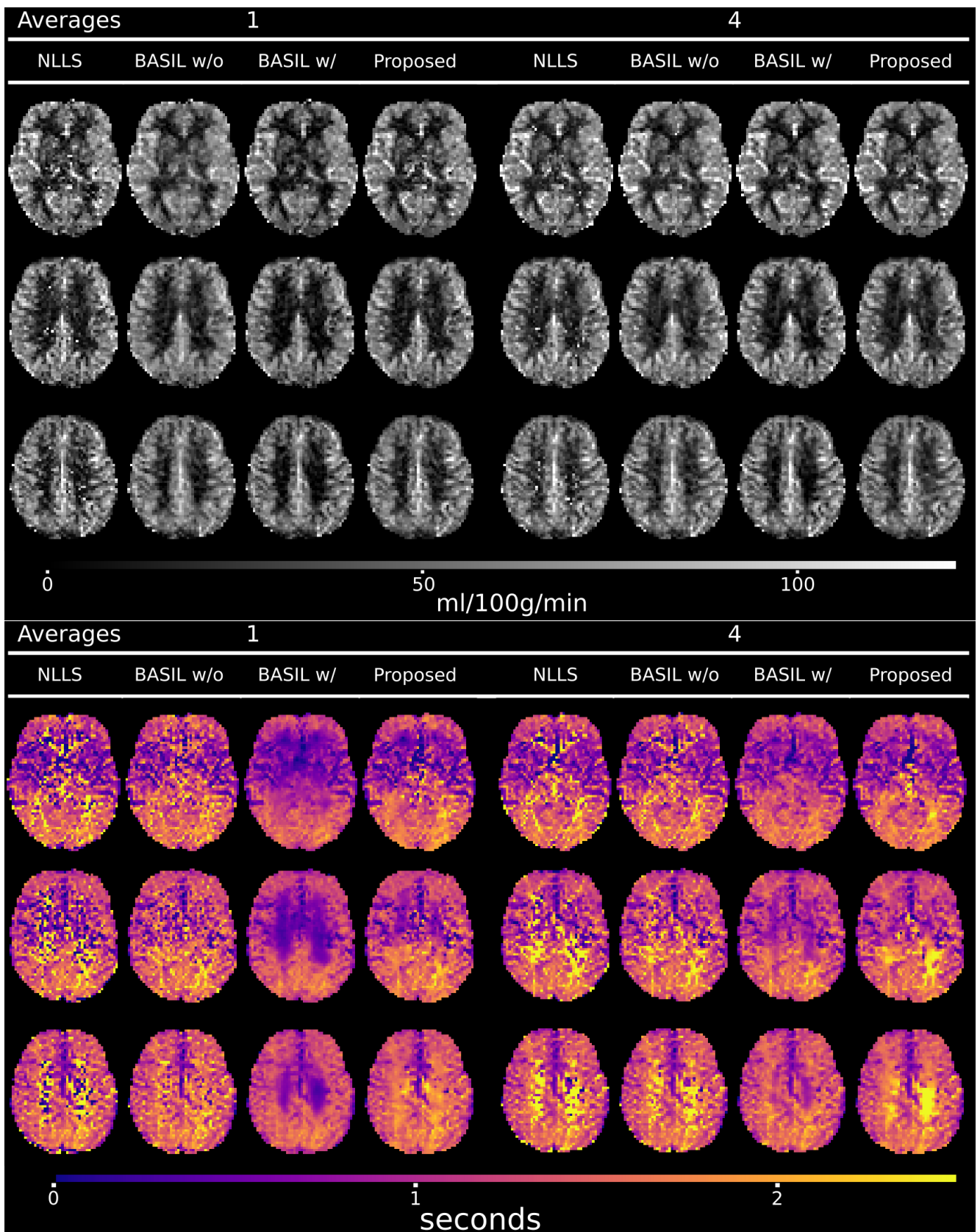
2012. PyCUDA and PyOpenCL: A scripting-based approach to GPU runtime code generation. *Parallel Computing* 38, 157–174. URL: <https://doi.org/10.1016/j.parco.2011.09.001>, doi:10.1016/j.parco.2011.09.001.
- Knoll, F., Bredies, K., Pock, T., Stollberger, R., 2010. Second order total generalized variation (TGV) for MRI. *Magnetic Resonance in Medicine* 65, 480–491. URL: <https://doi.org/10.1002/mrm.22595>, doi:10.1002/mrm.22595.
- Knoll, F., Holler, M., Koesters, T., Otazo, R., Bredies, K., Sodickson, D.K., 2017. Joint MR-PET reconstruction using a multi-channel image regularizer. *IEEE Transactions on Medical Imaging* 36, 1–16. URL: <https://doi.org/10.1109/tmi.2016.2564989>, doi:10.1109/tmi.2016.2564989.
- Liu, F., Velikina, J.V., Block, W.F., Kijowski, R., Samsonov, A.A., 2017. Fast realistic MRI simulations based on generalized multi-pool exchange tissue model. *IEEE Transactions on Medical Imaging* 36, 527–537. URL: <https://doi.org/10.1109/tmi.2016.2620961>, doi:10.1109/tmi.2016.2620961.
- Lu, H., Clingman, C., Golay, X., van Zijl, P.C., 2004. Determining the longitudinal relaxation time (T1) of blood at 3.0 tesla. *Magnetic Resonance in Medicine* 52, 679–682. URL: <https://doi.org/10.1002/mrm.20178>, doi:10.1002/mrm.20178.
- Lustig, M., Donoho, D., Pauly, J.M., 2007. Sparse MRI: The application of compressed sensing for rapid MR imaging. *Magnetic Resonance in Medicine* 58, 1182–1195. URL: <https://doi.org/10.1002/mrm.21391>, doi:10.1002/mrm.21391.
- MacIntosh, B., Lindsay, A., Kylintireas, I., Kuker, W., Günther, M., Robson, M., Kennedy, J., Choudhury, R., Jezzard, P., 2010. Multiple inflow pulsed arterial spin-labeling reveals delays in the arterial arrival time in minor stroke and transient ischemic attack. *American Journal of Neuroradiology* 31, 1892–1894. URL: <https://doi.org/10.3174/ajnr.a2008>, doi:10.3174/ajnr.a2008.
- MacIntosh, B., Swardfager, W., Robertson, A., Tchistiakova, E., Saleem, M., Oh, P., Herrmann, N., Stefanovic, B., Lanctôt, K., 2014. Regional cerebral arterial transit time hemodynamics correlate with vascular risk factors and cognitive function in men with coronary artery disease. *American Journal of Neuroradiology* 36, 295–301. URL: <https://doi.org/10.3174/ajnr.a4094>, doi:10.3174/ajnr.a4094.
- Maier, O., Schloegl, M., Bredies, K., Stollberger, R., 2019. 3D Model-Based Parameter Quantification on Resource Constrained Hardware using Double-Buffering, in: *Proc. 27th Annu. Meet. ISMRM, Montréal, QC, Canada*, p. 4839.
- Maier, O., Schoormans, J., Schloegl, M., Strijkers, G.J., Lesch, A., Benkert, T., Block, T., Coolen, B.F., Bredies, K., Stollberger, R., 2018. Rapid T1 quantification from high resolution 3d data with model-based reconstruction. *Magnetic Resonance in Medicine* 81, 2072–2089. URL: <https://doi.org/10.1002/mrm.27502>, doi:10.1002/mrm.27502.
- Maier, O., Spann, S.M., Bödenler, M., Stollberger, R., 2020. Pyqmri: An accelerated python based quantitative mri toolbox. *Journal of Open Source Software* 5, 2727. URL: <https://doi.org/10.21105/joss.02727>, doi:10.21105/joss.02727.
- Maleki, N., Dai, W., Alsop, D.C., 2011. Optimization of background suppression for arterial spin labeling perfusion imaging. *Magnetic Resonance Materials in Physics, Biology and Medicine* 25, 127–133. URL: <https://doi.org/10.1007/s10334-011-0286-3>, doi:10.1007/s10334-011-0286-3.
- Malitsky, Y., Pock, T., 2018. A first-order primal-dual algorithm with line-search. *SIAM Journal on Optimization* 28, 411–432. URL: <https://doi.org/10.1137/16m1092015>, doi:10.1137/16m1092015.
- Mehranian, A., McGinnity, C.J., Neji, R., Prieto, C., Hammers, A., Vita, E.D., Reader, A.J., 2020. Motion-corrected and high-resolution anatomically assisted (MOCHA) reconstruction of arterial spin labeling MRI. *Magnetic Resonance in Medicine* 84, 1306–1320. URL: <https://doi.org/10.1002/mrm.28205>, doi:10.1002/mrm.28205.
- Mutsaerts, H.J., Petr, J., Václavů, L., van Dalen, J.W., Robertson, A.D., Caan, M.W., Masellis, M., Nederveen, A.J., Richard, E., MacIntosh, B.J., 2017. The spatial coefficient of variation in arterial spin labeling cerebral blood flow images. *Journal of Cerebral Blood Flow & Metabolism* 37, 3184–3192. URL: <https://doi.org/10.1177/0271678x16683690>, doi:10.1177/0271678x16683690.
- Roeloffs, V., Wang, X., Sumpf, T.J., Untenberger, M., Voit, D., Frahm, J., 2016. Model-based reconstruction for T1 mapping using single-shot inversion-recovery radial FLASH. *International Journal of Imaging Systems and Technology* 26, 254–263. URL: <https://doi.org/10.1002/ima.22196>, doi:10.1002/ima.22196.
- Roemer, P.B., Edelstein, W.A., Hayes, C.E., Souza, S.P., Mueller, O.M., 1990. The NMR phased array. *Magnetic Resonance in Medicine* 16, 192–225. URL: <https://doi.org/10.1002/mrm.1910160203>, doi:10.1002/mrm.1910160203.
- Rudin, L.I., Osher, S., Fatemi, E., 1992. Nonlinear total variation based noise removal algorithms. *Physica D: Nonlinear Phenomena* 60, 259–268. URL: [https://doi.org/10.1016/0167-2789\(92\)90242-f](https://doi.org/10.1016/0167-2789(92)90242-f), doi:10.1016/0167-2789(92)90242-f.
- Salzo, S., Villa, S., 2012. Convergence analysis of a proximal newton method. *Computational Optimization and Applications* 53, 557–589. URL: <https://doi.org/10.1007/s10589-012-9476-9>, doi:10.1007/s10589-012-9476-9.
- Smith, S.M., 2002. Fast robust automated brain extraction. *Human Brain Mapping* 17, 143–155. URL: <https://doi.org/10.1002/hbm.10062>, doi:10.1002/hbm.10062.
- Smith, S.M., Jenkinson, M., Woolrich, M.W., Beckmann, C.F., Behrens, T.E., Johansen-Berg, H., Bannister, P.R., Luca, M.D., Drobnjak, I., Flitney, D.E., Niazy, R.K., Saunders, J., Vickers, J., Zhang, Y., Stefano, N.D., Brady, J.M., Matthews, P.M., 2004. Advances in functional and structural MR image analysis and implementation as FSL. *NeuroImage* 23, S208–S219. URL: <https://doi.org/10.1016/j.neuroimage.2004.07.051>, doi:10.1016/j.neuroimage.2004.07.051.
- Spann, S.M., Shao, X., Wang, D.J., Aigner, C.S., Schloegl, M., Bredies, K., Stollberger, R., 2020. Robust single-shot acquisition of high resolution whole brain ASL images by combining time-dependent 2d CAIPR-INHA sampling with spatio-temporal TGV reconstruction. *NeuroImage* 206, 116337. URL: <https://doi.org/10.1016/j.neuroimage.2019.116337>, doi:10.1016/j.neuroimage.2019.116337.
- Spann, S.M., Shao, X., Wang, D.J., Aigner, C.S., Schloegl, M., Bredies, K., Stollberger, R., 2019. Improving temporal resolution of 3D Arterial Spin Labeling perfusion imaging by combining CAIPRINHA encoding and spatio-temporal TGV reconstruction, in: *Proc. 27th Annu. Meet. ISMRM, Montréal, QC, Canada*, p. 0841.
- Stone, J.E., Gohara, D., Shi, G., 2010. OpenCL: A parallel programming standard for heterogeneous computing systems. *Computing in Science & Engineering* 12, 66–73. URL: <https://doi.org/10.1109/mcse.2010.69>, doi:10.1109/mcse.2010.69.
- Telischak, N.A., Detre, J.A., Zaharchuk, G., 2014. Arterial spin labeling MRI: Clinical applications in the brain. *Journal of Magnetic Resonance Imaging* 41, 1165–1180. URL: <https://doi.org/10.1002/jmri.24751>, doi:10.1002/jmri.24751.
- Tikhonov, A.N., Arsenin, V.I.A., 1977. *Solutions of ill-posed problems / Andrey N. Tikhonov and Vasilii Y. Arsenin ; translation editor, Fritz John. Winston ; distributed solely by Halsted Press Washington : New York.*
- Verbree, J., van Osch, M.J.P., 2017. Influence of the cardiac cycle on pCASL: cardiac triggering of the end-of-labeling. *Magnetic Resonance Materials in Physics, Biology and Medicine* 31, 223–233. URL: <https://doi.org/10.1007/s10334-017-0611-6>, doi:10.1007/s10334-017-0611-6.
- Vidorreta, M., Wang, Z., Rodríguez, I., Pastor, M.A., Detre, J.A., Fernández-Seara, M.A., 2013. Comparison of 2d and 3d single-shot ASL perfusion fMRI sequences. *NeuroImage* 66, 662–671. URL: <https://doi.org/10.1016/j.neuroimage.2012.10.087>, doi:10.1016/j.neuroimage.2012.10.087.
- Wang, X., Roeloffs, V., Klosowski, J., Tan, Z., Voit, D., Uecker, M., Frahm, J., 2017. Model-based T1 mapping with sparsity constraints using single-shot inversion-recovery radial FLASH. *Magnetic Resonance in Medicine* 79, 730–740. URL: <https://doi.org/10.1002/mrm.26726>, doi:10.1002/mrm.26726.
- Wang, Z., 2012. Improving cerebral blood flow quantification for arterial spin labeled perfusion MRI by removing residual motion artifacts and global signal fluctuations. *Magnetic Resonance Imaging* 30, 1409–1415. URL: <https://doi.org/10.1016/j.mri.2012.05.004>, doi:10.1016/j.mri.2012.05.004.
- Wang, Z., Aguirre, G.K., Rao, H., Wang, J., Fernández-Seara, M.A., Childress, A.R., Detre, J.A., 2008. Empirical optimization of ASL data analysis using an ASL data processing toolbox: ASLtbx. *Magnetic Resonance Imaging* 26, 261–269. URL: <https://doi.org/10.1016/j.mri.2007.07.003>, doi:10.1016/j.mri.2007.07.003.
- Woods, J.G., Chappell, M.A., Okell, T.W., 2018. A general framework for optimizing arterial spin labeling MRI experiments. *Magnetic Resonance*

- in *Medicine* 81, 2474–2488. URL: <https://doi.org/10.1002/mrm.27580>, doi:10.1002/mrm.27580.
- Woolrich, M.W., Jbabdi, S., Patenaude, B., Chappell, M., Makni, S., Behrens, T., Beckmann, C., Jenkinson, M., Smith, S.M., 2009. Bayesian analysis of neuroimaging data in FSL. *NeuroImage* 45, S173–S186. URL: <https://doi.org/10.1016/j.neuroimage.2008.10.055>, doi:10.1016/j.neuroimage.2008.10.055.
- Ye, F.Q., Frank, J.A., Weinberger, D.R., McLaughlin, A.C., 2000. Noise reduction in 3d perfusion imaging by attenuating the static signal in arterial spin tagging (ASSIST). *Magnetic Resonance in Medicine* 44, 92–100. URL: [https://doi.org/10.1002/1522-2594\(200007\)44:1<92::aid-mrm14>3.0.co;2-m](https://doi.org/10.1002/1522-2594(200007)44:1<92::aid-mrm14>3.0.co;2-m), doi:10.1002/1522-2594(200007)44:1<92::aid-mrm14>3.0.co;2-m.
- Zaharchuk, G., 2012. Arterial spin labeling for acute stroke: Practical considerations. *Translational Stroke Research* 3, 228–235. URL: <https://doi.org/10.1007/s12975-012-0159-8>, doi:10.1007/s12975-012-0159-8.
- Zaharchuk, G., Bammer, R., Straka, M., Shankaranarayan, A., Alsop, D.C., Fischbein, N.J., Atlas, S.W., Moseley, M.E., 2009. Arterial spin-label imaging in patients with normal bolus perfusion-weighted MR imaging findings: Pilot identification of the borderzone sign. *Radiology* 252, 797–807. URL: <https://doi.org/10.1148/radiol.2523082018>, doi:10.1148/radiol.2523082018.
- Zhang, Y., Brady, M., Smith, S., 2001. Segmentation of brain MR images through a hidden markov random field model and the expectation-maximization algorithm. *IEEE Transactions on Medical Imaging* 20, 45–57. URL: <https://doi.org/10.1109/42.906424>, doi:10.1109/42.906424.

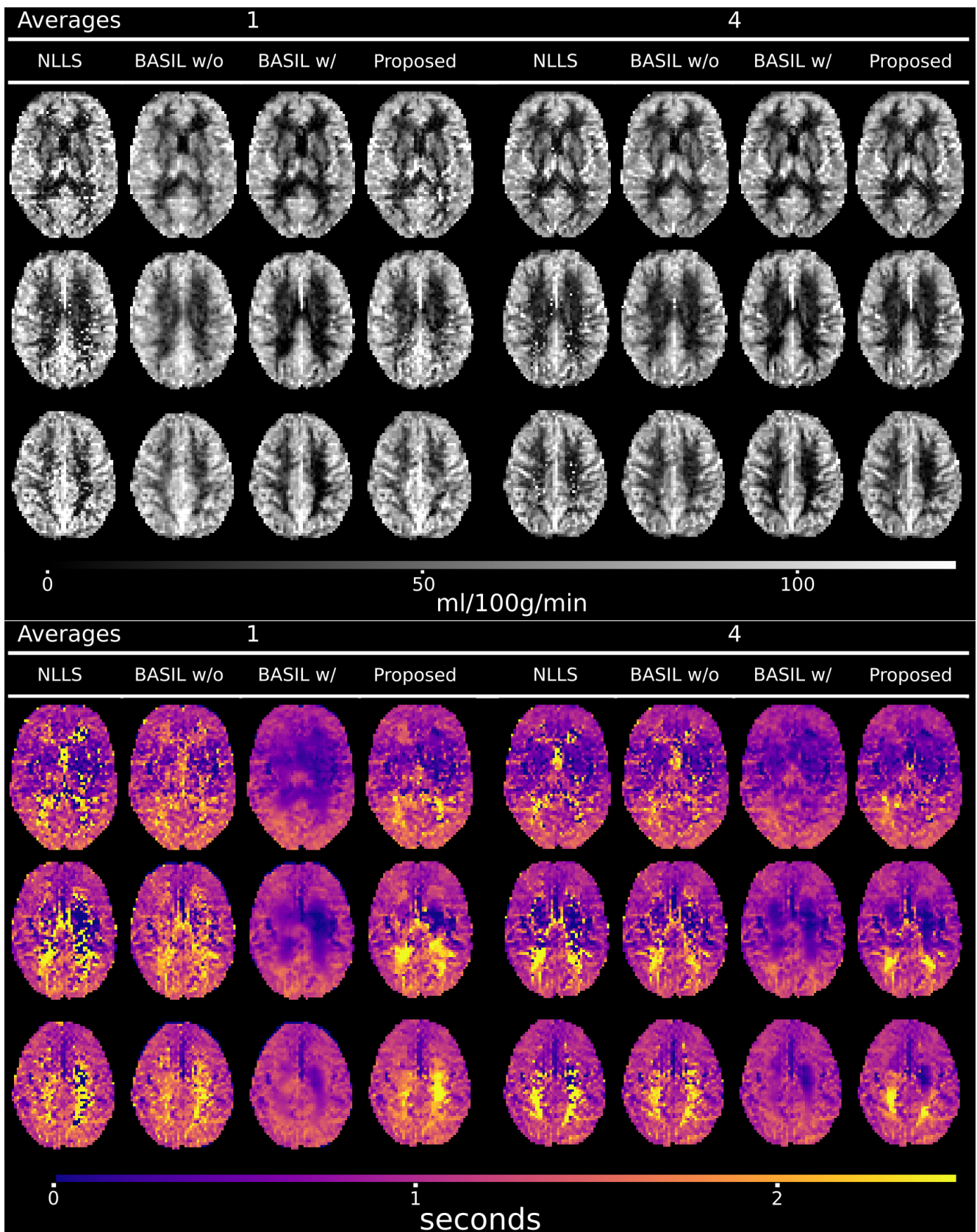
Supplementary Material



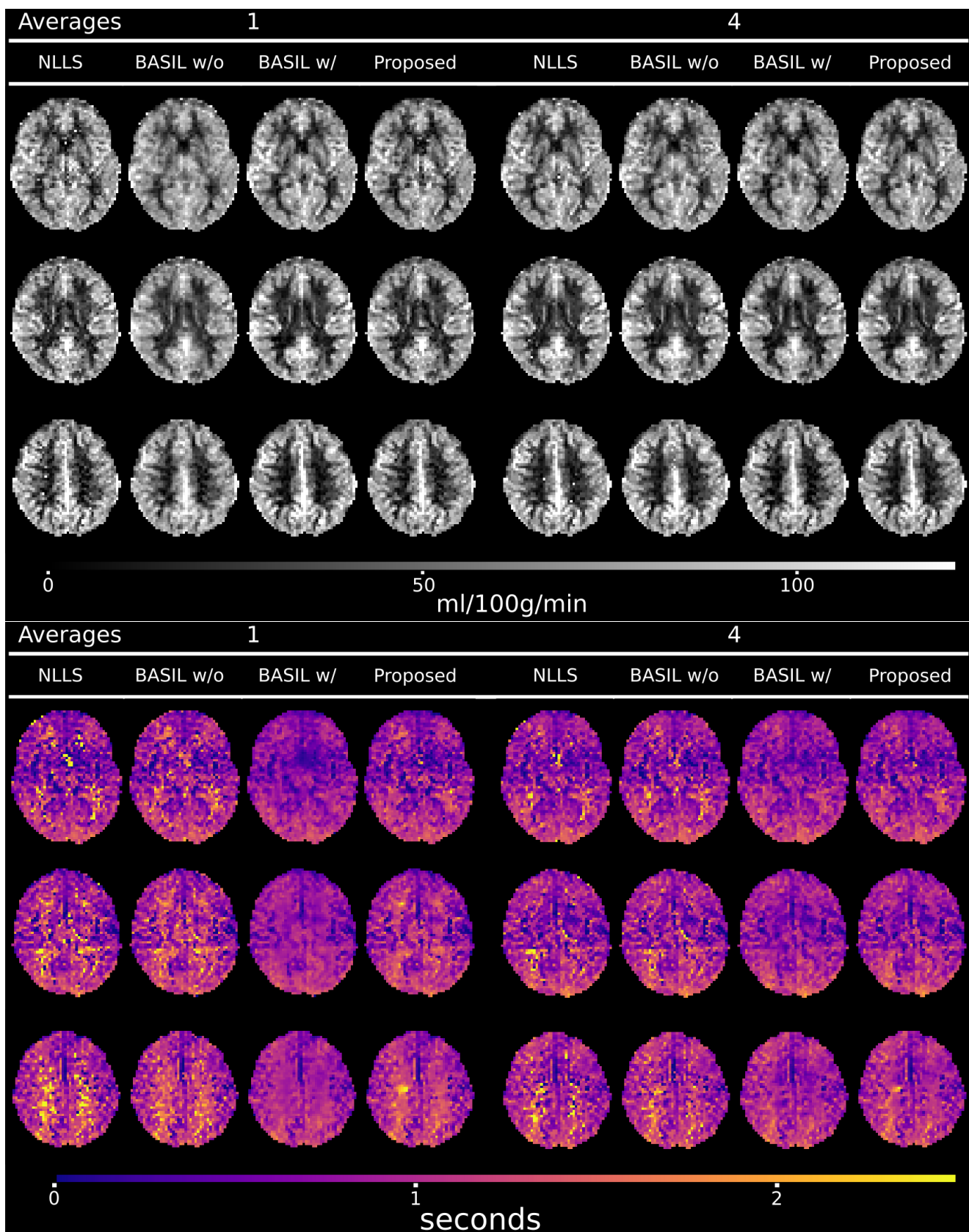
Supplementary Material Figure S1. Three representative slices of the CBF and ATT maps of subject 1



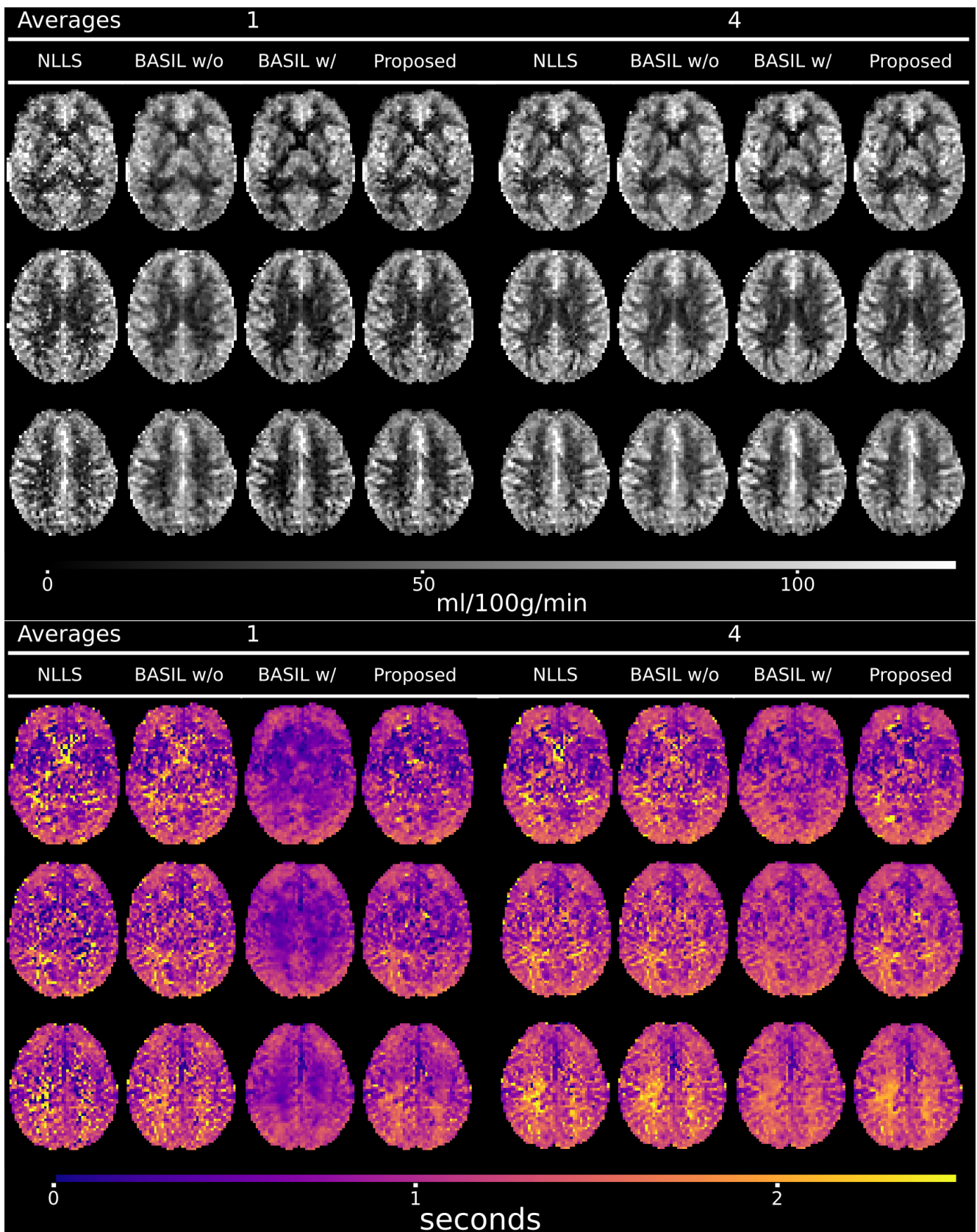
Supplementary Material Figure S2. Three representative slices of the CBF and ATT maps of subject 2



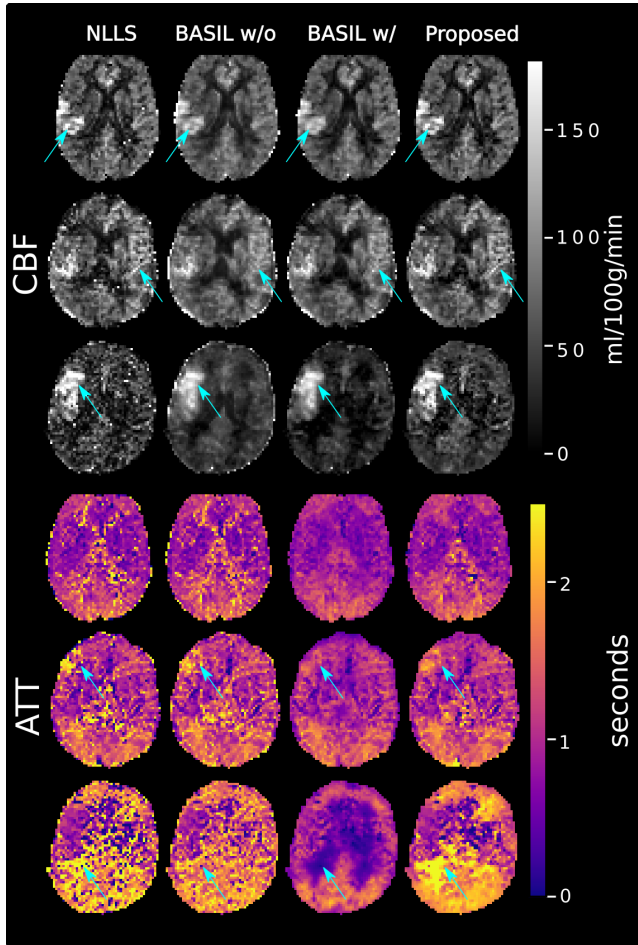
Supplementary Material Figure S3. Three representative slices of the CBF and ATT maps of subject 4



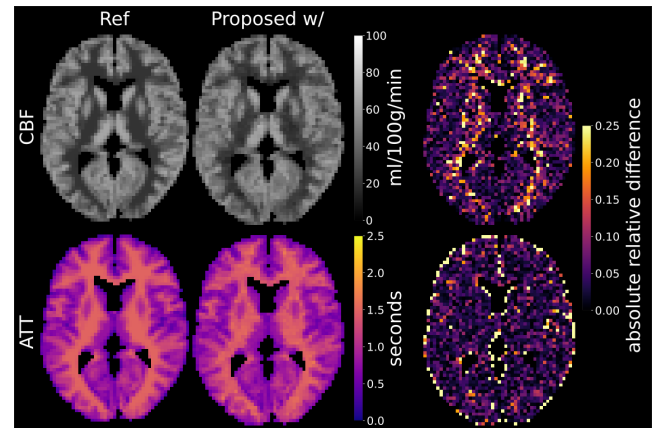
Supplementary Material Figure S4. Three representative slices of the CBF and ATT maps of subject 5



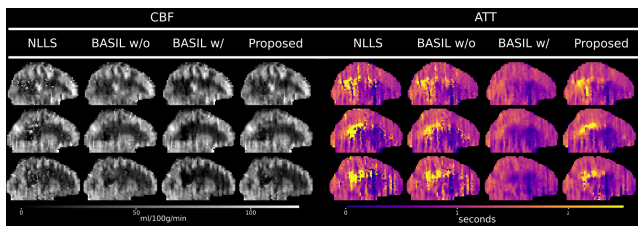
Supplementary Material Figure S5. Three representative slices of the CBF and ATT maps of subject 6



Supplementary Material Figure S6. An exemplary slice of CBF and ATT for the remaining stroke patients. Patients are shown in rows, different reconstruction methods in columns. Difference between methods are highlighted by arrows.



Supplementary Material Figure S8. Preliminary results for a 2D slice-by-slice PASL based quantification model. Shown is an exemplary slice of Case 1. Simulated resolution amounted to $3 \times 3 \times 6 \text{ mm}^3$. As a 2D acquisition is assumed, a time delay between subsequent slices is introduced.



Supplementary Material Figure S7. Three exemplary sagittal views of healthy subject 3, showing the blurring induced in z-direction due to long echo train length.